Publication Year	2023
Acceptance in OA	2025-02-25T14:52:23Z
Title	Gaia Data Release 3. Analysis of RVS spectra using the General Stellar Parametriser from spectroscopy
Authors	Recio-Blanco, A., de Laverny, P., Palicio, P. A., Kordopatis, G., Álvarez, M. A., Schultheis, M., Contursi, G., Zhao, H., Torralba Elipe, G., Ordenovic, C., Manteiga, M., Dafonte, C., Oreshina-Slezak, I., Bijaoui, A., Frémat, Y., Seabroke, G., Pailler, F., Spitoni, E., POGGIO, Eloisa, Creevey, O. L., Abreu Aramburu, A., Accart, S., Andrae, R., Bailer-Jones, C. A. L., Bellas-Velidis, I., Brouillet, N., BRUGALETTA, Elisa, Burlacu, A., Carballo, R., Casamiquela, L., Chiavassa, A., Cooper, W. J., Dapergolas, A., Delchambre, L., Dharmawardena, T. E., DRIMMEL, Ronald, Edvardsson, B., Fouesneau, M., Garabato, D., García-Lario, P., García-Torres, M., Gavel, A., Gomez, A., González-Santamaría, I., Hatzidimitriou, D., Heiter, U., Jean-Antoine Piccolo, A., Kontizas, M., Korn, A. J., LANZAFAME, Alessandro, Lebreton, Y., Le Fustec, Y., Licata, E. L., Lindstrøm, H. E. P., Livanou, E., Lobel, A., Lorca, A., Magdaleno Romeo, A., Marocco, F., Marshall, D. J., Mary, N., Nicolas, C., Pallas-Quintela, L., Panem, C., Pichon, B., Riclet, F., Robin, C., Rybizki, J., Santoveña, R., Silvelo, A., SMART, Richard Laurence, Sarro, L. M., SORDO, Rosanna, Soubiran, C., Süveges, M., Ulla, A., VALLENARI, Antonella, Zorec, J., Utrilla, E., Bakker, J.
Publisher's version (DOI)	10.1051/0004-6361/202243750
Handle	http://hdl.handle.net/20.500.12386/36218
Journal	ASTRONOMY & ASTROPHYSICS
Volume	674

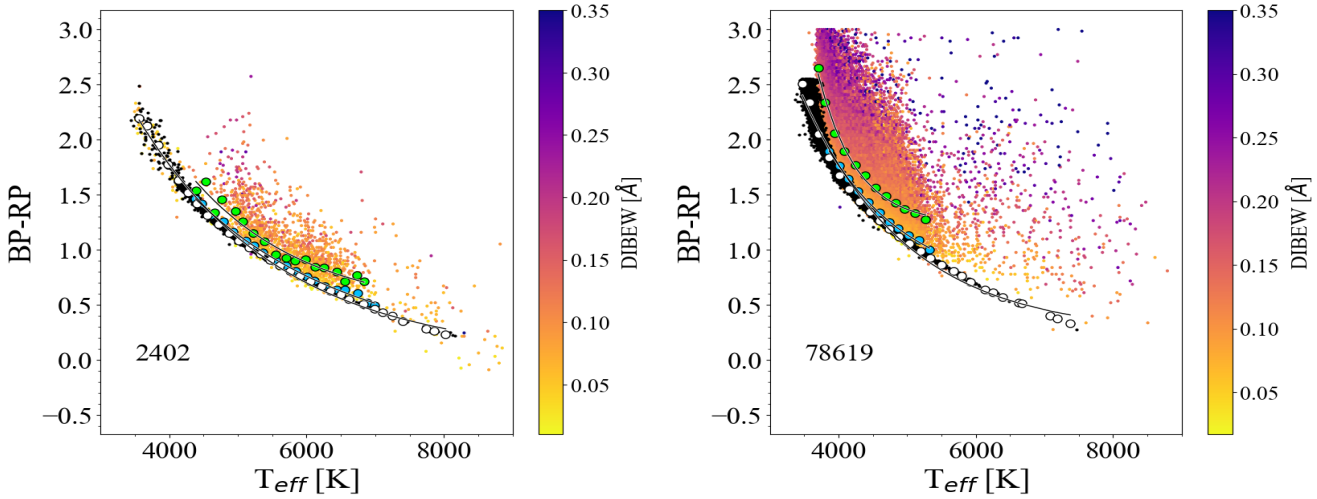

Fig. 19. Trend of (BP-RP) colour with GSP-Spec effective temperature produced by the MatisseGauguin workflow for dwarfs (*left panel*) and giants (*right panel*). The colour code indicates the estimated DIB EW, which increases with interstellar absorption (the DIB flag has been imposed to be equal to zero). Blue circles show the median values of the distribution for the stars with a DIB EW lower than 0.05 Å. Green circles are the median values for stars whose DIB EW is equal to the median value of the distribution (0.07 Å for dwarf stars on the *left panel*, and 0.12 Å for giants on the right panel), plus a dispersion of ±0.01 Å. Black dots (and white circles) are the values (and their median) predicted by the Casagrande et al. (2021) relation, assuming no extinction.

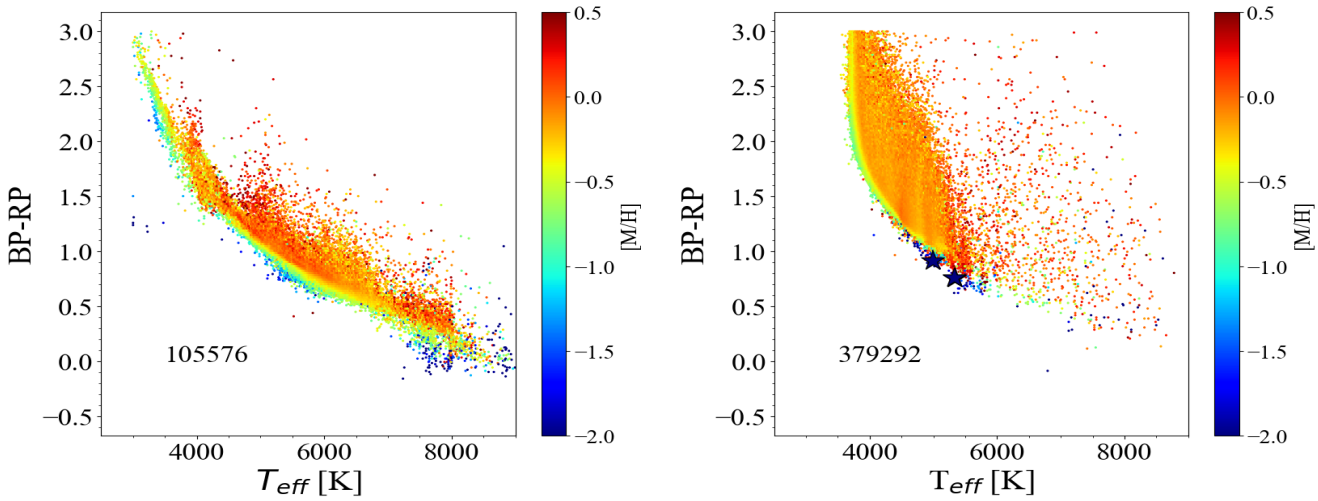

Fig. 20. Same as Fig. 19 but using the estimated stellar metallicity [M/H] as colour code. The selected stars have the first 13 quality flags in the gspspec flagging chain equal to zero. Two extremely metal-poor stars, discussed in Sect. 10.5, are indicated by star symbols. The number of stars is indicated in each panel.

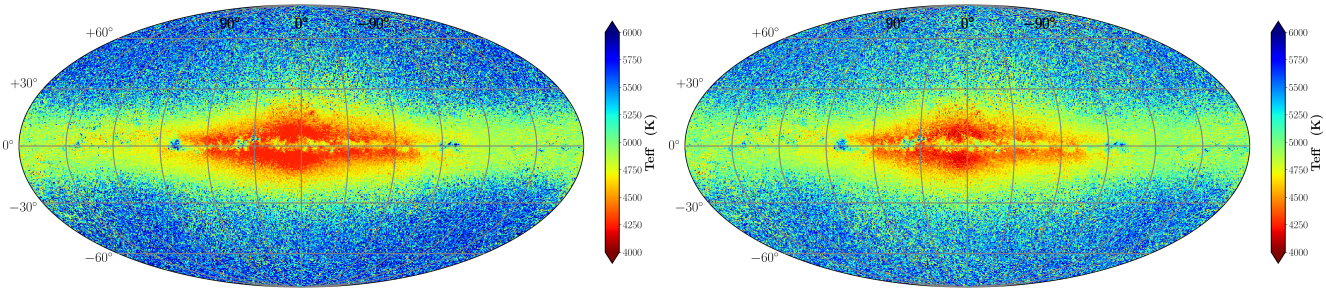

Fig. 21. Milky Way as revealed by the GSP-Spec effective temperature estimated by MatisseGauguin (*left*) and ANN (*right*). These HEALPix maps in Galactic coordinates have a spatial resolution of 0.46°. The colour code corresponds to the median of $T_{\rm eff}$ in each pixel.

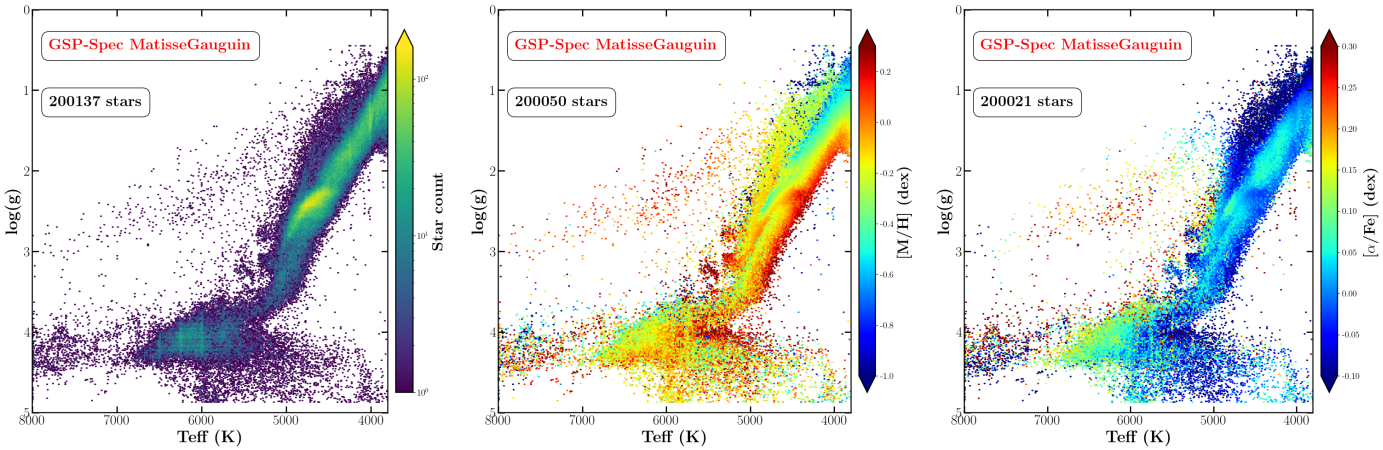

Fig. 22. Kiel diagrams for the MatisseGauguin output parameters (stored in the main DR3 astrophysical parameters table) for high-quality spectra ($S/N > 150$) and excluding high-rotating stars ($vbroadT = vbroadG = vbroadM = 0$) and possibly misclassified very cool giants ($KMtypestars = 0$). The colour codes of the different panels show the stellar density (*left panel*) and the median of [M/H] and [α/Fe] per point (*central and right panels*, respectively). The proposed log(g) and [α/Fe] calibrations are applied.

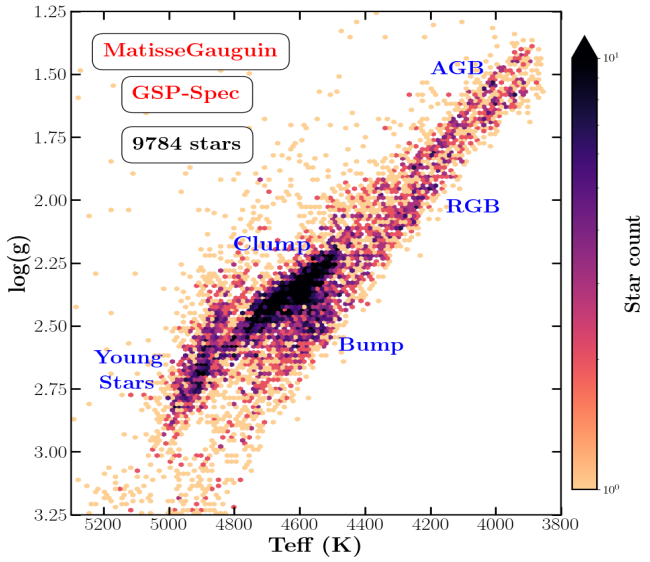

Fig. 23. Zoom onto the MatisseGauguin Kiel diagram for stars in a very restricted metallicity domain, $-0.05 < [M/H] < 0.00$ dex, and with high-quality spectra. The RGB and AGB sequences appear as two resolved parallel tracks. The very close-by RGB bump and HB clump are also isolated. A sequence of young stars (with ages of less than ~1 Gyr) can be identified in the hotter side, with an overdensity at around $T_{\rm eff} \sim 5000$ K. These are second red clump objects, i.e. massive stars burning He in their core.

(5 576 282 stars, left panel) and their ANN effective temperature (5 524 387 stars, right panel). Both figures show the giant star population dominating the Galactic disc and bulge regions. The in-plane interstellar extinction pattern can also be noticed by its effect on the underlying parameterised populations: in higher extinction regions, cool giant stars observable at large distances become too faint in the RVS wavelength domain, and the median of the temperature distribution becomes hotter. Finally, nearby fainter dwarf stars in the foreground dominate the regions above and below the Galactic plane, increasing the median $T_{\rm eff}$ values. It can be observed that ANN provides lower temperatures for these stars. For more details on the GSP-Spec selection function, we refer to Gaia Collaboration (2023a) (see their Sect. 3).

10.4. Atmospheric parameters of high-S/N spectra

To illustrate the GSP-Spec atmospheric parameter estimates in the high-S/N regime, we selected all the stars with $S/N > 150$, excluding high-rotating stars and potentially misclassified cool giants (imposing $vbroadT$=$vbroadG$=$vbroadM = 0$ and $KMtypestars = 0$, respectively). This selects a sample of nearly 202 000 stars.

Figure 22 presents the MatisseGauguin parametrisation of the selected objects in different Kiel diagrams colour coded according to stellar density (left panel), [M/H] (middle panel), and [α/Fe] (right panel). We applied the log(g) calibration proposed in Sect. 9 and the [α/Fe] calibration reported in Table 4 (fourth-order polynomial, without applying the suggested cuts in log(g) in order to show a complete Kiel diagram). The parameters precision can be assessed from the well-defined evolutionary sequences. For instance, the clearly distinguishable red clump presents a metallicity dependence that is independent from that of the red giant branch, as expected. Additionally, younger, more massive stars populate the hotter metal-rich sequence with logg $\lesssim 3$. These stars are located in the Milky Way spiral arms (cf. Gaia Collaboration 2023a). It is worth noting that, in the high-S/N regime, the algorithm shows overfitting patterns (overdensity features at the reference grid points). This can be observed in the left panel of Fig. 22 for the $T_{\rm eff}$. The log(g) values are not affected in this figure because they have been calibrated.

The precision of the Matisse-Gauguin atmospheric parameters (without any use of astrometric inputs) can also be appreciated from Fig. 23, which shows a zoom into the Kiel diagram of the stars in a very restricted metallicity domain, $-0.05 < [M/H] < 0.00$ dex (defined using the upper and lower confidence values in the form `mh_gspspec_upper`< 0.00 dex and `mh_gspspec_lower`> -0.05 dex). In addition, only stars with $T_{\rm eff}$>3750 K, $KMgiantPar = 0$ and `logchisq_gspspec`<–3.75 were selected so as to avoid classification problems at the very cool end of the giant branch. It can be appreciated that the RGB bump[18] is resolved as an overdensity feature at $T_{\rm eff} \sim 4600$ K and log(g) ~ 2.5. The very high

[18] The RGB bump corresponds to the arrival of the narrow burning H-shell to the sharp chemical discontinuity in the H-distribution profile caused by the penetration of the convective envelope.

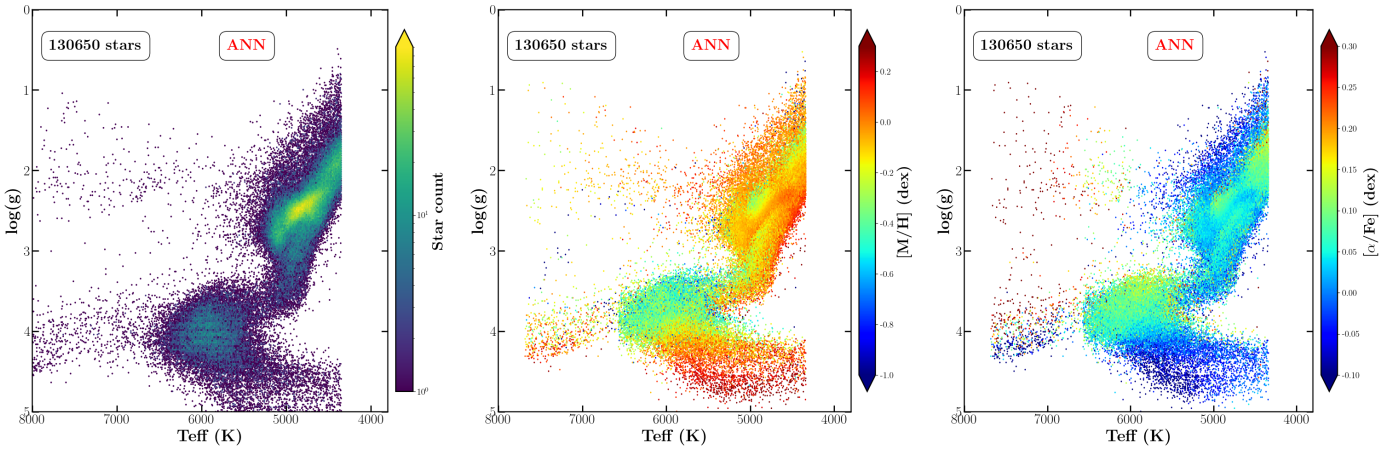

Fig. 24. Same as Fig. 22 but for the ANN output parameters (stored in the supplementary DR3 astrophysical parameters table). In this case, we imposed that the first eight quality flags in Sect. 8 be equal to zero. The calibrations proposed in Sect. 9.2 were applied. Although a larger dispersion is observed with respect to MatisseGauguin, a general agreement exists, supporting the coherence of the two methodologically independent analysis.

parameter precision allows us to separate this RGB feature from the nearby horizontal branch clump visible as a narrow elongated feature between $4500 < T_{\rm eff} < 4800$ K and $2.20 < \log(g) < 2.50$. Moreover, Fig. 23 shows the capability of these very high-quality GSP-Spec parameters to disentangle the extremely close-by red giant branch and asymptotic giant branch sequences, which appear as two parallel tracks for $\log(g) < 2.25$. Finally, the overdensity located around $T_{\rm eff} \sim 5000$ K and $2.50 < \log(g) < 2.80$ corresponds, as mentioned above, to the evolutionary sequence of young stars of about less than 1 Gyr (cf. Gaia Collaboration 2023a for a more detailed analysis of these stars tracing the disc spiral arms). This will put important constraints on stellar evolution models, and specifically on the mass and metallicity dependencies of the red clump, the RGB bump, and the RGB and AGB behaviours.

Figure 24 shows the ANN results for the same stars, after imposing that the first eight quality flags in Sect. 8 be equal to zero and the four parameter calibrations proposed in Sect. 9.2. On one hand, a general agreement is observed with respect to MatisseGauguin. In particular, a well-defined Red Clump and a comparable metallicity trend for giant stars are observed, although with a higher dispersion and an underabundance of metal-poor stars in ANN results ([M/H] ≤ -1.0 dex, partly explainable by the temperature cut in the cool regime due to calibration boundaries). On the other hand, the metallicity and [α/Fe] distributions differ from the MatisseGauguin one for dwarf stars, presenting an unexpected trend with gravity. Despite the higher dispersion of ANN parameters, its overall agreement with MatisseGauguin brings support to the coherence of the two methodologically independent analyses.

Additionally, Fig. 25 shows the [α/Fe] versus [M/H] distribution from the MatisseGauguin analysis for the selected high-S/N spectra, applying the suggested cuts in $\log(g)$ for the [α/Fe] calibration and imposing $T_{\rm eff} \leq 6000$ K and $vbroad \leq 10$ km s^{-1}. These last two filters help to control the quality of the [α/Fe] by reducing second-order temperature trends and refining the filtering performed by the $vbroadT$, $vbroadG$, and $vbroadM$ flags. The halo and disc sequences can be observed, with the thick disc sequence joining the thin disc one at a metallicity of around -0.4 dex. It is also worth noting that, as expected from chemical evolution models, the thin disc sequence continues to decrease at supersolar metallicities. As shown in

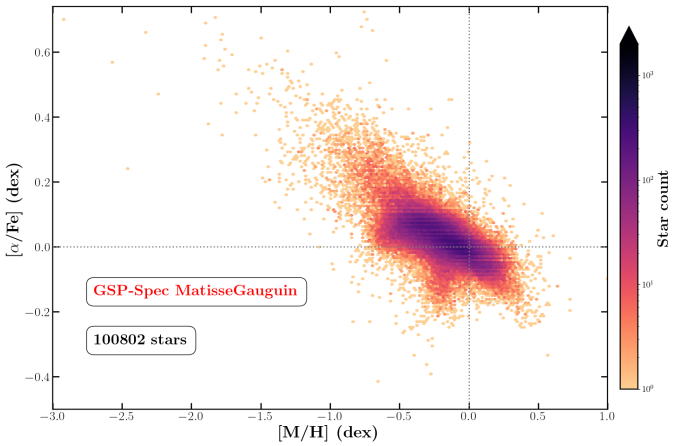

Fig. 25. [α/Fe] versus [M/H] for the same MatisseGauguin stars as in Fig. 22 but applying the recommended gravity interval for the calibration (Table 4) and imposing $T_{\rm eff} \leq 6000$ K and $vbroad \leq 10$ km s^{-1}.

Gaia Collaboration (2023a), the [α/Fe] clearly correlates with the kinematical properties of stellar populations. Moreover, the *Gaia*-Enceladus sequence of accreted stars (Helmi et al. 2018) is also distinguishable (lower [α/Fe] values than those for typical thick discs and halos in the metal-poor regime). Finally, a group of low-[α/Fe] stars at a metallicity of about [M/H] ~ -0.4 dex is also visible. This corresponds to young massive stars in the spiral arms (for a discussion about the chemical properties of these stars see, Gaia Collaboration 2023a). It is worth noting that, as mentioned in Sect. 9, GSP-Spec [α/Fe] estimates are dominated by the [Ca/Fe] abundance. We refer to Gaia Collaboration (2023a) for a detailed illustration of individual α-element abundances, including Mg, Ca, Si, S, and Ti, as well as other chemical species including N, iron-peak elements, and heavy elements.

10.5. Parametrisation of extremely metal-poor stars

Metal-poor stars are relics of the most ancient formation epochs of the Milky Way, and in particular, they are crucial for disentangling the sequence of satellite mergers contributing to the Galaxy build-up (e.g. Helmi 2020). For this reason, they are

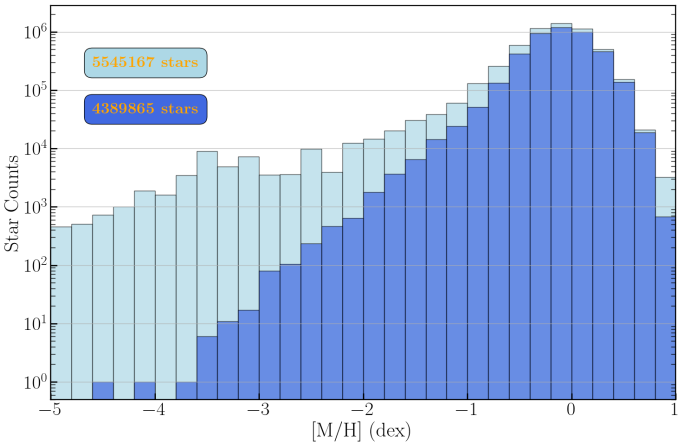

Fig. 26. Metallicity distributions for the MatisseGauguin parametrised stars. The light-blue histogram refers to the whole sample without any filtering. The medium-blue histogram presents a very strict filtering selecting stars with the best derived metallicities (see associated text for more details).

the priviledged targets of several spectroscopic surveys from the ground like Pristine (Starkenburg et al. 2017). However, the lack of spectral signatures in metal-poor spectra reduces the information on the stellar parameters, increasing the uncertainties and making their parametrisation challenging. In the following, we illustrate the GSP-Spec capabilities to parametrise not only metal-poor, but also ultra-metal-poor ([M/H] < −3.0 dex) stars, providing suggestions on the necessary filters to apply.

Figure 26 shows the GSP-Spec MatisseGauguin metallicity distribution in a logarithmic scale. The light-blue histogram refers to the complete sample without any quality filtering. In this distribution, which is useful for a rough stellar selection, there are about 66 000 stars with [M/H] ≤ −2.0 dex. It is nevertheless observed that the profile of the histogram is unexpectedly flat in the ultra-metal-poor regime. This is due to the $T_{\rm eff}$ limitations of the GSP-Spec reference spectra grid ($T_{\rm eff} \leq 8000$ K) inducing a $T_{\rm eff}$–[M/H] degeneracy. This problem can be satisfactorily resolved, as shown by the medium-blue histogram, by (i) disregarding the [M/H] values for stars with the first six characters of the GSP-Spec flagging chain ≥2, which limits the parameterisation biases, (ii) filtering out the metallicities of stars with *extrapol* flag (eighth character of the flagging chain) ≥3, which limits the extrapolation issues, (iii) eliminating the ultra-metal-poor stars hotter than 6000 K, which conservatively filters out metallicities with unreliable uncertainties due to border effects (in $T_{\rm eff}$ and [M/H]), and (iv) filtering out possible remaining GSP-Spec misclassifications of very hot stars with stellar types O and B as estimated by the Extended Stellar Parameteriser of Hot Stars (ESP-HS) and reported in the *AstrophysicalParameters* table as *spectraltype_esphs*. To complete the previous filters, which are optimised for the very metal-poor regime, the medium-blue histogram of Fig. 26 filters out the metallicities of stars with $T_{\rm eff} < 3500$ or $\log(g) > 4.9$ or *KMgiantPar* > 0. The filtering implemeted by the *KMgiantPar* flag, which controls the quality of the parameterisation of very cool giants, can be slightly extended, as reported in Gaia Collaboration (2023a), disregarding the metallicity of stars with $T_{\rm eff} < 4150$ K and $2.4 < \log(g) < 3.8$. Thanks to these different quality filters, the medium-blue histogram presented in Fig. 26 recovers the expected decrease in the number of stars in the very metal-poor regime, reporting only very reliable results within the corresponding uncertainties. Among these, there are about 300 with [M/H] < –2.5 dex and about 40 stars with [M/H] < –3.0 dex.

To confirm that GSP-Spec is indeed able to correctly estimate the parameters of very metal-poor and ultra-metal-poor stars, we show the RVS spectrum of two of them, which were randomly chosen among the highest S/N spectra (Figs. 27 and 28). The very few lines present in these spectra are extremely weak (except those of Ca II) and, as a consequence, no individual abundances were derived for both stars. [M/H] is therefore estimated only from very few available weak calcium or iron lines. The careful visual inspection of the synthetic spectra fit of the corresponding RVS spectra corroborates the very metal-poor nature of both stars.

We first validated the atmospheric parameters of *Gaia* DR3 6268770373590148224 (Fig. 27, [M/H] = –3.19 dex) by computing several synthetic spectra with parameters found within the upper and lower MatisseGauguin uncertainties, i.e. between 5097 and 5456 dex for $T_{\rm eff}$ and [2.38, 2.76] for $\log(g)$. The parameter values are confirmed within the uncertainties. The global fit is excellent and [M/H] is indeed found between the published range [−3.6, −2.7]. We note again that this rather large range of [M/H] is caused by the quasi absence of lines in its RVS spectrum. We also checked the literature for this star and found it to be known as the peculiar star HD 140283, already studied in several articles, the first one going back about 70 years (Chamberlain & Aller 1951). Its most recent published parameters seem to converge towards a slightly hotter star with the majority of published [M/H] being found around −2.5 dex, in agreement with our estimates taking into account the literature error bars. Its [α/Fe] value of 0.56 dex and its kinematical parameters (a Galactic azimuthal velocity of ∼29 km s^{-1}, as taken from Gaia Collaboration 2023a) make this star a typical halo representative.

The second example, *Gaia* DR3 6477295296414847232, is shown in Fig. 28. This star has [M/H] = −3.52 dex (and confidence values between −3.94 dex and −3.17 dex), a $T_{\rm eff}$ of 4994 K (with confidence values between 4781 K and 5071 K) and a $\log(g)$ of 2.13 (with confidence values between 1.5 and 2.26). Again, this parameterisation is confirmed by visual inspection of the spectrum fit in Fig. 28. Additionally, to exclude [M/H] values higher than the reported upper confidence level ([M/H] =–3.07 dex), Fig. 28 includes a synthetic spectrum (in orange) corresponding to [M/H] = –2.5 dex, which clearly overestimates the CaII and Fe lines depth and width and confirms that a lower metallicity is required, as in the one estimated by GSP-Spec. Finally, the literature inspection of this object, identified as the peculiar star HD 2000654, leads to 23 different metallicity estimates with a median value of −2.9 dex ± 0.25 dex, in agreement with our results. It is interesting to note that Roederer et al. (2014) and Hansen et al. (2018) classify this star has an *r*-process enhanced object of *r–I* type, with a metallicity of −3.13 dex and −2.91 dex, respectively. In addition, based on high-resolution spectra, Roederer et al. (2014) reports a [Ca/Fe] = 0.47 dex ± 0.17 in agreement with our calibrated [α/Fe] = 0.62 dex, a carbon abundance of [C/Fe] = 0.31 dex, and a nitrogen abundance of [N/Fe] = −0.4 dex. More recently, Placco et al. (2018), using medium-resolution spectra, classify this star as a CEMP-II object, with a carbon enhancement of [C/Fe] = 0.71 dex. It is important to remark that no sign of carbon enhancement, perturbing the metallicity estimate, is present in the RVS spectra due to the absence of CH molecular lines. In summary, the literature results again validate the GSP-Spec parameterisation of this ultra-metal-poor star, including its [α/Fe] estimates.

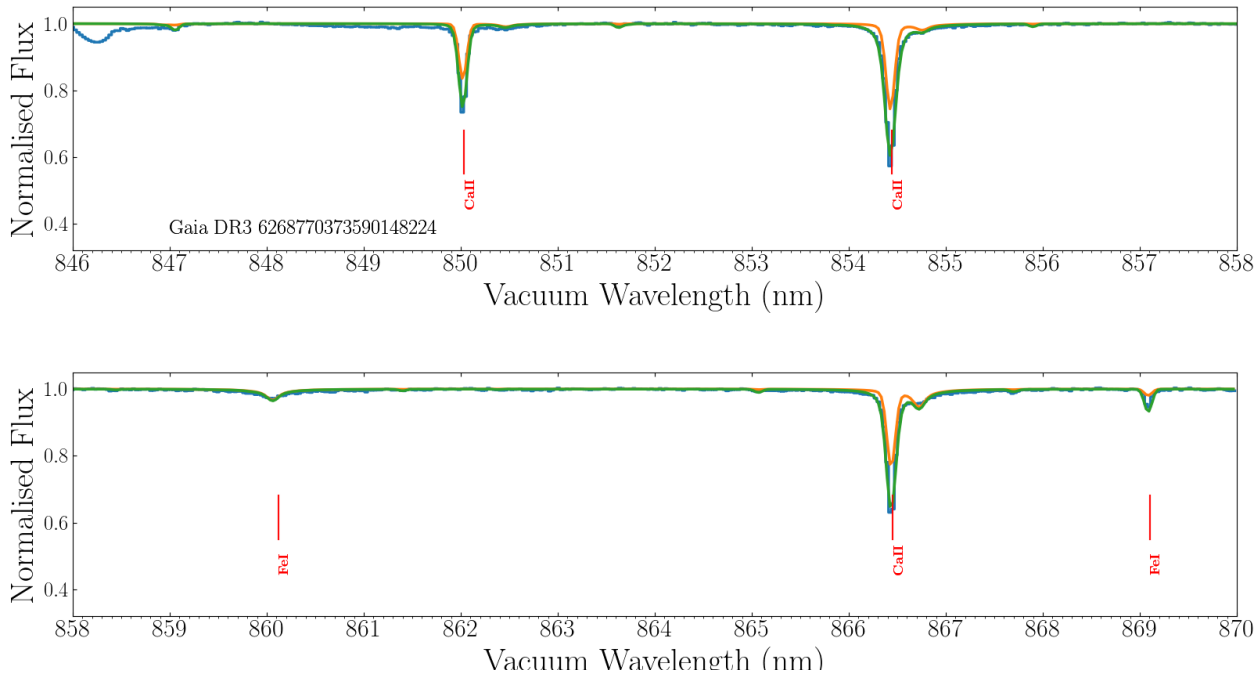

Fig. 27. RVS spectrum (blue histogram) of the very metal-poor star *Gaia* DR3 6268770373590148224 whose MatisseGauguin atmospheric parameters are $T_{\rm eff} = 5331$ K, $\log(g) = 2.54$, [M/H] = −3.19 dex, and [α/Fe] = 0.56 dex (S/N = 419). The model spectra correspond to the lower and upper [M/H] values (−3.60 and −2.71 dex in orange and green, respectively). No rotational profile was applied (suspected low-rotating star). See text for more details.

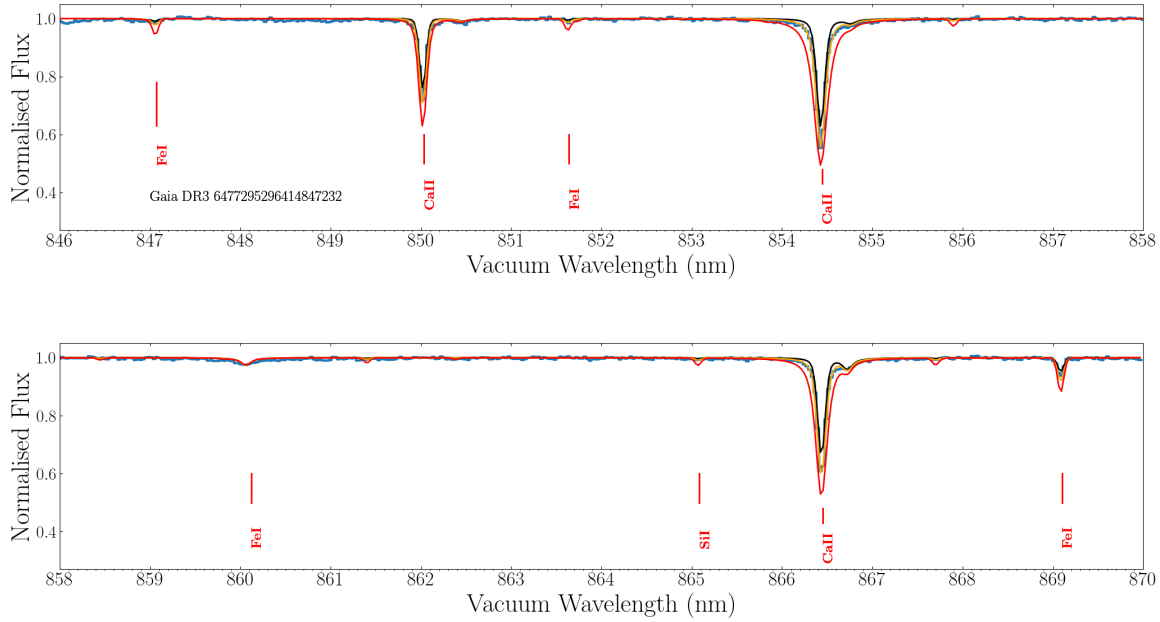

Fig. 28. RVS spectrum (blue histogram) of the ultra-metal-poor star *Gaia* DR3 6477295296414847232 whose MatisseGauguin atmospheric parameters are $T_{\rm eff} = 4994$ K $\log(g) = 2.13$, [M/H] = −3.52 dex, and [α/Fe] = 0.68 dex (S/N = 236). The model spectra correspond to the lower and upper [M/H] values (−3.52 and −3.07 dex in black and orange, respectively). A spectrum with [M/H] = −2.5 dex is also shown (red line) to definitively exclude such higher metallicities. No rotational profiles were considered.

11. Summary and conclusions

Here, we summarise the stellar parametrisation of *Gaia* RVS spectra performed by the GSP-Spec module and published as part of *Gaia* DR3. The goals, the input data, the used methodologies, and the validation are presented in detail. The resulting catalogues are published in the *AstrophysicalParameters* table (for the GSP-Spec MatisseGauguin workflow, including stellar atmospheric parameters, individual chemical abundances, a cyanogen differential EW, and DIB feature parameters), and in the *AstrophysicalParametersSupp* (for the ANN workflow providing atmospheric parameters). The GSP-Spec catalogue flags are also carefully defined and guidance for their use is illustrated with examples. We highly recommend future users of the GSP-Spec parameters to adopt these flags for their specific science cases.

With about 5.6 million stars, the *Gaia* DR3 GSP-Spec all-sky catalogue is the largest compilation of stellar chemo-physical parameters ever published and the first of its kind based on data acquired in space. The extreme homogeneity of the analysis combined with continuous data collection for almost three years enable a careful spectroscopic data reduction, a detailed modelling of systematic errors, and consequently, higher number statistics and a parametrisation quality that is comparable to that of ground-based surveys of higher spectral resolution and wavelength coverage.

GSP-Spec parameters open new horizons in stellar, Galactic, and insterstellar medium studies. In addition to the scientific performance analysis of GSP-Spec data published in Gaia Collaboration (2023a,b), we illustrate the precision of the parameters here with (i) the colour–temperature relation, (ii) the Kiel diagrams and the [α/Fe] vs. [M/H] distribution in the high-S/N regime ($S/N > 150$, more than 2 million stars), (iii) our ability to disentangle different evolutionary stages of giant stars that are extremely close-by in the parameter space (RGB/AGB, bump/clump), and finally, (iv) a demonstration of the capability of GSP-Spec in the challenging parametrisation of metal-poor and extremely metal-poor stars.

Finally, it is worth noting that, as GSP-Spec is one of the parametrisation modules activated at the end of the DPAC analysis chain, this *Gaia* third data release is actually the first GSP-Spec data release. The acquired experience will benefit future releases, for which the number of parametrised stars will be a factor of ten larger (~50 million stars) as a result of the spectra S/N increase with observing time. It is important to note that the present data set is already at least a factor 8 larger than previous individual ground-based catalogues and a factor 3 larger than their very heterogeneous joint compilation. GSP-Spec is therefore exploring Galactic regions that we had previously only hypothesised from models (based on low number statistics). Thanks to the *Gaia* RVS GSP-Spec chemo-physical parametrisation, we now have a privileged view of the sky from beyond Earth.

Acknowledgements. This work presents results from the European Space Agency (ESA) space mission *Gaia* (https://www.cosmos.esa.int/gaia). *Gaia* data are processed by the *Gaia* Data Processing and Analysis Consortium (DPAC). Funding for the DPAC is provided by national institutions, in particular the institutions participating in the *Gaia* MultiLateral Agreement (MLA). The *Gaia* archive website is https://archives.esac.esa.int/gaia. Acknowledgments from the financial institutions are given in Appendix H. We sincerely thank the stellar atmosphere group in Uppsala for providing the MARCS model atmospheres, B. Plez for having developped and maintaining the TURBOSPECTRUM package and, M. Bergemann for providing before publication the adopted relation between microturbulent velocity and atmospheric parameters. We also thank A. Bragaglia for her comments on the manuscript and the anonymous referee for very useful comments and suggestions. Finally, part of the calculations have been performed with the high-performance computing facility SIGAMM, hosted by the Observatoire de la Côte d'Azur. We acknowledge financial supports from the french space agency (CNES), Agence National de la Recherche (ANR 14-CE33-014-01) and Programmes Nationaux de Physique Stellaire & Cosmologie et Galaxies (PNPS & PNCG) of CNRS/INSU. ES, ARB, PdL, GK and MS acknowledge funding from the European Union's Horizon 2020 research and innovation program under SPACE-H2020 grant agreement number 101004214 (EXPLORE project).

References

Abdurro'uf, A. K., Aerts, C., Silva Aguirre, V., et al. 2022, ApJS, 259, 35
Allende Prieto, C. 2016, Astron. Nachr., 337, 837
Allende Prieto, C., Beers, T. C., Wilhelm, R., et al. 2006, ApJ, 636, 804
Andrae, R., Fouesneau, A., Sordo, R., et al. 2023, A&A, 674, A27 (*Gaia* DR3 SI)
Bailer-Jones, C. A. L., Andrae, R., Arcay, B., et al. 2013, A&A, 559, A74
Bijaoui, A., Recio-Blanco, A., de Laverny, P., & Ordenovic, C. 2010, in ADA 6- Sixth Conference on Astronomical Data Analysis, J. L. Starck, M. Saber Naceur, & R. Murtagh, 9
Bijaoui, A., Recio-Blanco, A., de Laverny, P., & Ordenovic, C. 2012, Stat. Method. - Elsevier, 9, 55
Birch, K. P., & Downs, M. J. 1994, Metrologia, 31, 315
Buder, S., Sharma, S., Kos, J., et al. 2021, MNRAS, 506, 150
Cannon, A. J., & Pickering, E. C. 1918, Ann. Harvard College Obs., 91, 1
Cantat-Gaudin, T., Anders, F., Castro-Ginard, A., et al. 2020, A&A, 640, A1
Casagrande, L., Lin, J., Rains, A. D., et al. 2021, MNRAS, 507, 2684
Castro-Ginard, A., Jordi, C., Luri, X., et al. 2022, A&A, 661, A118
Catmull, E., & Rom, R. 1974, in Computer Aided Geometric Design, R. E. Barnhill, & R. F. Riesenfeld (Academic Press), 317
Chamberlain, J. W., & Aller, L. H. 1951, ApJ, 114, 52
Contursi, G., de Laverny, P., Recio-Blanco, A., & Palicio, P. A. 2021, A&A, 654, A130
Creevey, O., Sordo, R., Pailler, F., et al. 2023, A&A, 674, A26 (*Gaia* DR3 SI)
Cropper, M., Katz, D., Sartoretti, P., et al. 2018, A&A, 616, A5
Dafonte, C., Fustes, D., Manteiga, M., et al. 2016, A&A, 594, A68
de Laverny, P., Recio-Blanco, A., Worley, C. C., & Plez, B. 2012, A&A, 544, A126
de Laverny, P., Recio-Blanco, A., Worley, C. C., et al. 2013, The Messenger, 153, 18
Forsberg, R., Jönsson, H., Ryde, N., & Matteucci, F. 2019, A&A, 631, A113
Gaia Collaboration (Recio-Blanco, A., et al.) 2023a, A&A, 674, A38 (*Gaia* DR3 SI)
Gaia Collaboration (Schultheis, M., et al.) 2023b, A&A, 674, A40 (*Gaia* DR3 SI)
Gaia Collaboration (Vallenari, A., et al.) 2023c, A&A, 674, A1 (*Gaia* DR3 SI)
Gershman, S. J., & Blei, D. M. 2012, J. Math. Psychol., 56, 1
Gilmore, G., Randich, S., Asplund, M., et al. 2012, The Messenger, 147, 25
Gilmore, G., Randich, S., Worley, C. C.et al. 2022, A&A, 666, A120
Górski, K. M., Hivon, E., Banday, A. J., et al. 2005, ApJ, 622, 759
Grevesse, N., Asplund, M., & Sauval, A. J. 2007, Space Sci. Rev., 130, 105
Gustafsson, B., Edvardsson, B., Eriksson, K., et al. 2008, A&A, 486, 951
Hansen, T. T., Holmbeck, E. M., Beers, T. C., et al. 2018, ApJ, 858, 92
Helmi, A. 2020, ARA&A, 58, 205
Helmi, A., Babusiaux, C., Koppelman, H. H., et al. 2018, Nature, 563, 85
Hinkel, N. R., Timmes, F. X., Young, P. A., Pagano, M. D., & Turnbull, M. C. 2014, AJ, 148, 54
Jofré, P., Heiter, U., & Soubiran, C. 2019, ARA&A, 57, 571
Katz, D., Munari, U., Cropper, M., et al. 2004, MNRAS, 354, 1223
Katz, D., Sartoretti, P., Guerrier, A., et al. 2023, A&A, 674, A5 (*Gaia* DR3 SI)
Kordopatis, G., Recio-Blanco, A., de Laverny, P., et al. 2011, A&A, 535, A106
Kordopatis, G., Hill, V., Irwin, M., et al. 2013, A&A, 555, A12
Kos, J. 2017, MNRAS, 468, 4255
Majewski, S. R., Schiavon, R. P., Frinchaboy, P. M., et al. 2017, AJ, 154, 94
Manteiga, M., Ordóñez, D., Dafonte, C., & Arcay, B. 2010, PASP, 122, 608
Martell, S. L., Sharma, S., Buder, S., et al. 2017, MNRAS, 465, 3203
Morgan, W. W., Keenan, P. C., & Kellman, E. 1943, An Atlas of Stellar Spectra, With an Outline of Spectral Classification (Chicago: The University of Chicago press)
Nordström, B., Mayor, M., Andersen, J., et al. 2004, A&A, 418, 989
Perdigon, J., de Laverny, P., Recio-Blanco, A., et al. 2021, A&A, 647, A162
Placco, V. M., Beers, T. C., Santucci, R. M., et al. 2018, AJ, 155, 256
Plez, B. 2012, Astrophysics Source Code Library [record ascl:1205.004]
Randich, S., Gilmore, G., Magrini, L., et al. 2022, A&A, 666, A121
Recio-Blanco, A. 2014, in Setting the scene for Gaia and LAMOST, eds. S. Feltzing, G. Zhao, N. A. Walton, & P. Whitelock, 298, 366
Recio-Blanco, A., Bijaoui, A., & de Laverny, P. 2006, MNRAS, 370, 141
Recio-Blanco, A., de Laverny, P., Kordopatis, G., et al. 2014, A&A, 567, A5
Recio-Blanco, A., de Laverny, P., Allende Prieto, C., et al. 2016, A&A, 585, A93
Roederer, I. U., Preston, G. W., Thompson, I. B., et al. 2014, AJ, 147, 136
Santos-Peral, P., Recio-Blanco, A., de Laverny, P., Fernández-Alvar, E., & Ordenovic, C. 2020, A&A, 639, A140
Sartoretti, P., Katz, D., Cropper, M., et al. 2018, A&A, 616, A6
Soubiran, C., Brouillet, N., & Casamiquela, L. 2022, A&A, 663A4, 16
Starkenburg, E., Martin, N., Youakim, K., et al. 2017, MNRAS, 471, 2587
Steinmetz, M., Guiglion, G., McMillan, P. J., et al. 2020, AJ, 160, 83
Steinmetz, M., Zwitter, T., Siebert, A., et al. 2006, AJ, 132, 1645
Tarricq, Y., Soubiran, C., Casamiquela, L., et al. 2021, A&A, 647, A19
Wilkinson, M. I., Vallenari, A., Turon, C., et al. 2005, MNRAS, 359, 1306
Yanny, B., Rockosi, C., Newberg, H. J., et al. 2009, AJ, 137, 4377
Zhao, G., Zhao, Y.-H., Chu, Y.-Q., Jing, Y.-P., & Deng, L.-C. 2012, Res. Astron. Astrophys., 12, 723
Zhao, H., Schultheis, M., Recio-Blanco, A., et al. 2021, A&A, 645, A14

[1] Université Côte d'Azur, Observatoire de la Côte d'Azur, CNRS, Laboratoire Lagrange, Nice, France
[2] CIGUS CITIC – Department of Computer Science and Information Technologies, University of A Coruña, Campus de Elviña s/n, A Coruña 15071, Spain
[3] CIGUS CITIC, Department of Nautical Sciences and Marine Engineering, University of A Coruña, Paseo de Ronda 51, 15071 A Coruña, Spain
[4] Royal Observatory of Belgium, 3 Avenue circulaire, 1180 Brussels, Belgium
[5] Mullard Space Science Laboratory, University College London, Holmbury St Mary, Dorking, Surrey RH5 6NT, UK
[6] CNES Centre Spatial de Toulouse, 18 Avenue Edouard Belin, 31401 Toulouse Cedex 9, France
[7] ATG Europe for European Space Agency (ESA), Camino bajo del Castillo, s/n, Urbanizacion Villafranca del Castillo, Villanueva de la Cañada, 28692 Madrid, Spain
[8] Max Planck Institute for Astronomy, Königstuhl 17, 69117 Heidelberg, Germany
[9] National Observatory of Athens, I. Metaxa and Vas. Pavlou, Palaia Penteli 15236, Athens, Greece
[10] Laboratoire d'astrophysique de Bordeaux, Univ. Bordeaux, CNRS, B18N, allée Geoffroy Saint-Hilaire, 33615 Pessac, France
[11] INAF – Osservatorio Astrofisico di Catania, Via S. Sofia 78, 95123 Catania, Italy
[12] Telespazio for CNES Centre Spatial de Toulouse, 18 Avenue Edouard Belin, 31401 Toulouse Cedex 9, France
[13] Dpto. de Matemática Aplicada y Ciencias de la Computación, Univ. de Cantabria, ETS Ingenieros de Caminos, Canales y Puertos, Avda. de los Castros s/n, 39005 Santander, Spain
[14] GEPI, Observatoire de Paris, Université PSL, CNRS, 5 place Jules Janssen, 92190 Meudon, France
[15] Centre for Astrophysics Research, University of Hertfordshire, College Lane, AL10 9AB Hatfield, UK
[16] INAF – Osservatorio Astrofisico di Torino, Via Osservatorio 20, 10025 Pino Torinese (TO), Italy
[17] Institut d'Astrophysique et de Géophysique, Université de Liège, 19c, Allée du 6 Août, 4000 Liège, Belgium
[18] Theoretical Astrophysics, Division of Astronomy and Space Physics, Department of Physics and Astronomy, Uppsala University, Box 516, 751 20 Uppsala, Sweden
[19] European Space Agency (ESA), European Space Astronomy Centre (ESAC), Camino bajo del Castillo, s/n, Urbanizacion Villafranca del Castillo, Villanueva de la Cañada, 28692 Madrid, Spain
[20] Data Science and Big Data Lab, Pablo de Olavide University, 41013 Seville, Spain
[21] Department of Astrophysics, Astronomy and Mechanics, National and Kapodistrian University of Athens, Panepistimiopolis, Zografos, 15783 Athens, Greece
[22] Dipartimento di Fisica e Astronomia "Ettore Majorana", Università di Catania, Via S. Sofia 64, 95123 Catania, Italy
[23] LESIA, Observatoire de Paris, Université PSL, CNRS, Sorbonne Université, Université de Paris, 5 place Jules Janssen, 92190 Meudon, France
[24] Université Rennes, CNRS, IPR (Institut de Physique de Rennes) – UMR 6251, 35000 Rennes, France
[25] Niels Bohr Institute, University of Copenhagen, Juliane Maries Vej 30, 2100 Copenhagen Ø, Denmark
[26] DXC Technology, Retortvej 8, 2500 Valby, Denmark
[27] Aurora Technology for European Space Agency (ESA), Camino bajo del Castillo, s/n, Urbanizacion Villafranca del Castillo, Villanueva de la Cañada, 28692 Madrid, Spain
[28] IPAC, Mail Code 100-22, California Institute of Technology, 1200 E. California Blvd., Pasadena, CA 91125, USA
[29] IRAP, Université de Toulouse, CNRS, UPS, CNES, 9 Av. colonel Roche, BP 44346, 31028 Toulouse Cedex 4, France
[30] Thales Services for CNES Centre Spatial de Toulouse, 18 Avenue Edouard Belin, 31401 Toulouse Cedex 9, France
[31] Dpto. de Inteligencia Artificial, UNED, c/ Juan del Rosal 16, 28040 Madrid, Spain
[32] INAF – Osservatorio astronomico di Padova, Vicolo Osservatorio 5, 35122 Padova, Italy
[33] Institute of Global Health, University of Geneva, Geneva, Switzerland
[34] Applied Physics Department, Universidade de Vigo, 36310 Vigo, Spain
[35] Sorbonne Université, CNRS, UMR7095, Institut d'Astrophysique de Paris, 98bis bd. Arago, 75014 Paris, France

Appendix A: *GSP-Spec* and radial velocities

The number of stars missing radial velocities ($V_{\rm Rad}$) for different *GSP-Spec* parameters are provided in Table A.1. Parameters not listed are not missing any $V_{\rm Rad}$.

Table A.1. *GSP-Spec* and radial velocity statistics.

GSP-Spec parameter	# stars missing $V_{\rm Rad}$
teff_gspspec	95
logg_gspspec	95
mh_gspspec	84
alphafe_gspspec	83
fem_gspspec	9
sife_gspspec	6
cafe_gspspec	6
mgfe_gspspec	2
feiim_gspspec	2
sfe_gspspec	6

Appendix B: Atomic lines selected for the chemical analysis

This Appendix introduces the list of selected lines used in the determination of the chemical abundances. In Table B.1, we summarise the reference wavelength value of each atomic line, as well as the wavelength ranges considered for its abundance determination and second normalisation windows. We note that the reference wavelength (col. 2) can differ from the vacuum wavelength of the analysed atomic line in case of multiplets or broad lines. For instance, for the Ca II IR triplet transitions at 850.036, 854.444, and 866.452 nm, two Ca abundances have been derived from the wings of each line to avoid the line core that could not be well modelled. In those cases, col. 2 refers to one of the Ca II wings.

The following lines (denoted by an asterisk in Table B.1) have multiple lines within the same abundance determination window: (855.913, 855.916) for Si I; (867.082, 867.258, 867.297, 867.366) and (869.632, 869.701) for S I; (852.037, 852.069) for Ti I; (848.283, 848.296, 848.431), (851.641, 851.745, 851.751), (852.738, 852.901, 853.020) and (868.916, 869.101) for Fe I[19]; (851.368, 851.381, 851.375) for Ce II. For the Fe II line measured in hot star spectra (see Sect. 8.7.2), some blends of weak Fe I transitions may be present in cooler star spectra.

Table B.1. List of the atomic lines adopted for the determination of individual chemical abundances by *GSP-Spec*. Col. 2 refers to the reference wavelength of the analysed lines (see text for details). The abundance determination window corresponds to the interval $[\lambda^-_{ab}, \lambda^+_{ab}]$ (third and fourth column, respectively) while the refined normalisation window includes the wavelength range $[\lambda^-_{norm}, \lambda^+_{norm}]$ (fifth and sixth column, respectively). All the wavelengths are in nanometres and in the vacuum.

Elt	λ	λ^-_{ab}	λ^+_{ab}	λ^-_{norm}	λ^+_{norm}
N I	863.161	863.071	863.281	862.891	863.371
N I	868.579	868.489	868.699	868.309	868.939
Mg I	847.602	847.512	847.692	847.212	847.812
Si I	853.851	853.731	853.941	853.371	854.961
*Si I	855.916	855.856	856.036	855.376	856.156
Si I	868.872	868.782	868.992	868.602	869.232
*S I	867.258	866.988	867.378	866.898	867.998
*S I	869.701	869.551	869.821	869.281	869.971
Ca I	863.631	863.511	863.691	863.361	863.931
Ca II	849.856	849.706	849.976	849.586	850.276
Ca II	850.216	850.156	850.276	849.886	850.306
Ca II	854.264	854.114	854.384	853.544	854.864
Ca II	854.624	854.564	854.744	854.294	854.804
Ca II	866.272	866.152	866.332	866.002	866.572
Ca II	866.632	866.512	866.692	866.302	866.782
*Ti I	852.069	851.979	852.129	851.799	852.249
Ti I	857.209	857.119	857.269	856.999	857.359
Ti I	869.472	869.382	869.562	869.292	869.832
Cr I	855.118	855.058	855.208	854.878	855.478
Cr I	864.567	864.447	864.627	864.207	864.867
*Fe I	848.296	848.206	848.446	847.666	848.896
*Fe I	851.641	851.551	851.851	851.281	852.001
*Fe I	852.901	852.691	853.081	852.481	853.321
Fe I	857.416	857.296	857.506	856.876	858.166
Fe I	858.462	858.312	858.612	858.132	858.762
Fe I	862.397	862.277	862.517	862.127	862.697
Fe I	867.713	867.593	867.863	867.443	868.013
*Fe I	869.101	868.891	869.191	868.441	869.821
Fe II	858.794	858.764	858.824	858.254	859.274
Ni I	863.937	863.847	864.027	863.697	864.147
Zr II	852.748	852.658	852.838	852.388	853.018
*Ce II	851.375	851.285	851.465	851.015	851.555
Nd II	859.389	859.299	859.479	859.209	859.689

[19] Only the strongest transitions are provided for iron.

Appendix C: Definition of the *GSP-Spec* flags

The following tables include the detailed definition of the individual characters in the *GSP-Spec* quality flag chain presented in Table 2. In addition, Fig. C.1 illustrates the implemented modelling of parameter biases induced by rotational broadening, leading to the definition of *vbroad*T, *vbroad*G and *vbroad*M quality flags (cf. Sec. 8.1 and Table C.1). The particular case of effective temperature biases is illustrated. Finally, Fig. C.2 presents the validation flow chart associated with the definition of quality flags for the DIB parametrisation (cf. Sect. 8.9 and Table C.13).

Table C.1. Definition of the parameter flags considering potential biases due to rotational velocity and/or macroturbulence. These flags are part of the *flags_gspspec* string chain defined in Table 2.

Flag name	Condition	Flag value
vbroadT	ΔTeff>2000 K	Filtered all
	500< ΔTeff≤2000 K	Flag 2
	250< ΔTeff≤500 K	Flag 1
	ΔTeff≤250 K	Flag 0
vbroadG	Δlogg>2 dex	Filter all *except Teff & DIB if Teff>7000 K* Flag 9
	1< Δlogg≤2 dex	Flag 2
	0.5< Δlogg≤1 dex	Flag 1
	Δlogg≤0.5 dex	Flag 0
vbroadM	Δ[M/H]>2 dex	Filter [M/H] & [X/Fe] Flag 9
	0.5< Δ[M/H]≤2 dex	Flag 2
	0.25< Δ[M/H]≤0.5 dex	Flag 1
	Δ[M/H]≤0.25 dex	Flag 0

Table C.2. Same as Table C.1 but for the potential biases due to uncertainties in the radial velocity shift correction (see also Table 2).

Flag name	Condition	Flag value
vradT	ΔTeff>2000 K	Filter all
	500< ΔTeff≤2000 K	Flag 2
	250< ΔTeff≤500 K	Flag 1
	ΔTeff≤250 K	Flag 0
vradG	Δlogg>2 dex	Filter all *except Teff & DIB if Teff>7000 K* Flag 9
	1< Δlogg≤2 dex	Flag 2
	0.5< Δlogg≤1 dex	Flag 1
	Δlogg≤0.5 dex	Flag 0
vradM	Δ[M/H]>2 dex	Filter [M/H] & [X/Fe] Flag 9
	0.5< Δ[M/H]≤2 dex	Flag 2
	0.25< Δ[M/H]≤0.5 dex	Flag 1
	Δ[M/H]≤0.25 dex	Flag 0

Table C.3. Definition of the parameter flags considering potential biases due to uncertainties in the RVS flux (MatisseGauguin parametrisation; see also Table 2).

Flag name	Condition	Flag value
fluxNoise	σTeff>2000 K or σlogg>2 dex	Filter all Flag 9
	σTeff≤2000 K and σlogg≤2 dex and σ[M/H]>2 dex	Filter [M/H] & [X/Fe] Flag 5
	σTeff≤2000 K and σlogg≤2 dex and σ[M/H]≤2 dex and σ[α/Fe]>0.8 dex	Filter [α/Fe] & [X/Fe] Flag 4
	500< σTeff≤2000 K and 1< σlogg≤2 dex and 0.5< σ[M/H]≤2 dex and 0.2< σ[α/Fe]≤0.8 dex	Flag 3
	250< σTeff≤500 K and 0.5< σlogg≤1 dex and 0.25< σ[M/H]≤0.5 dex and 0.1< σ[α/Fe]≤0.2 dex	Flag 2
	100< σTeff≤250 K and 0.2< σlogg≤0.5 dex and 0.1< σ[M/H]≤0.25 dex and 0.05< σ[α/Fe]≤0.1 dex	Flag 1
	σTeff≤100 K and σlogg≤0.2 dex and σ[M/H]≤0.1 dex and σ[α/Fe]≤0.05 dex	Flag 0

Table C.4. Same as Table C.3 but for the ANN parametrisation.

ANN fluxNoise	
Condition	**Value**
$\sigma T_{\rm eff}$> 525 K or σlog(g)>0.9 or σ[M/H]>0.5 or σ[α/Fe]< 0.16 dex	Flag 9
225< $\sigma T_{\rm eff}$≤525 K and 0.4< σlog(g)≤0.9 or 0.19< σ[M/H]≤0.5 dex or 0.09< σ[α/Fe]≤0.16 dex	Flag 3
140< $\sigma T_{\rm eff}$≤225 K and 0.3< σlog(g)≤0.4 or 0.12< σ[M/H]≤0.19 dex or 0.06< σ[α/Fe]≤0.09 dex	Flag 2
100< $\sigma T_{\rm eff}$≤140 K and 0.24< σlog(g)≤0.3 or 0.09< σ[M/H]≤0.12 dex or 0.05< σ[α/Fe]≤0.06 dex	Flag 1
$\sigma T_{\rm eff}$≤100 K and σlog(g)≤0.24 and σ[M/H]≤0.09 dex and σ[α/Fe]≤0.05 dex	Flag 0

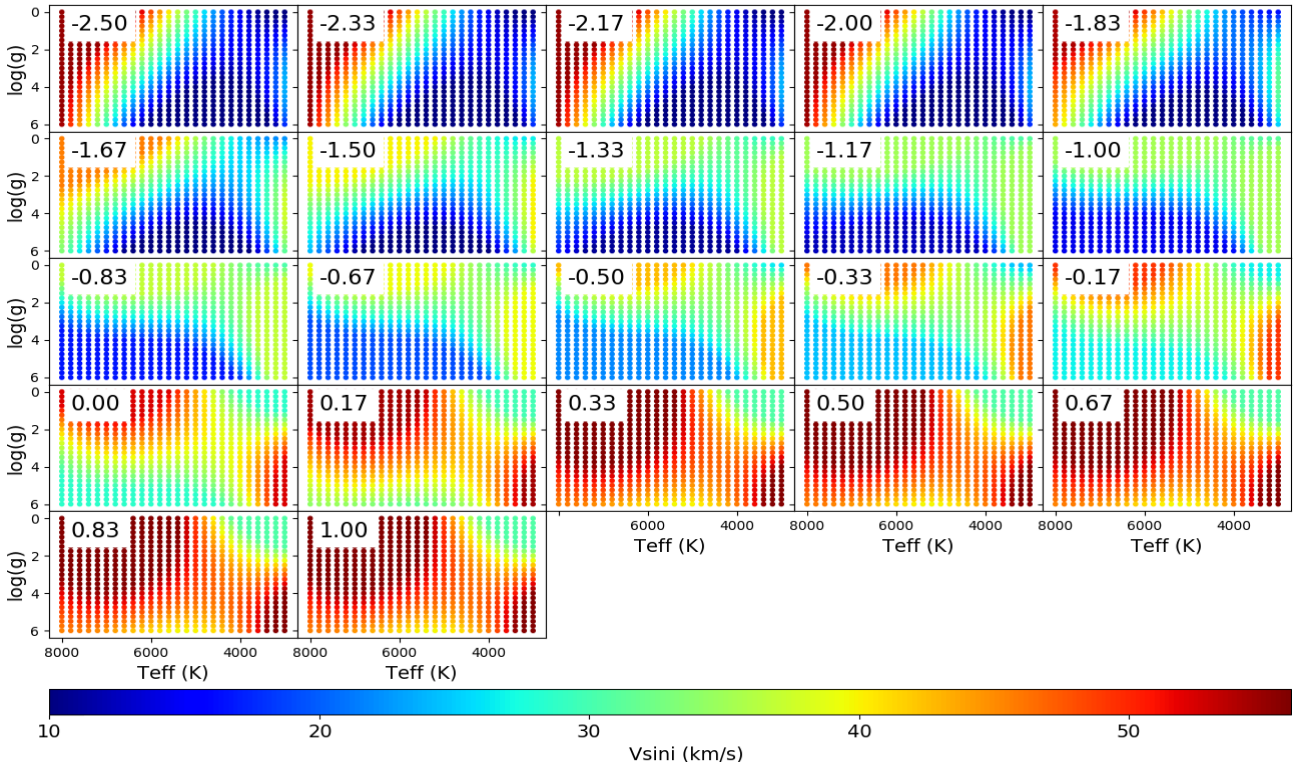

Fig. C.1. Limiting V sin i values (colour code) leading to a bias of 250< $\Delta T_{\rm eff}$≤500 K in the *GSP-Spec* parametrisation. This has been used to estimate the third-order polynomial with $T_{\rm eff}$, log(g), and [M/H] as variables used to define the *vbroad*T flag (equal to 1 in this example). The [M/H] values for each panel are indicated in their upper right corner.

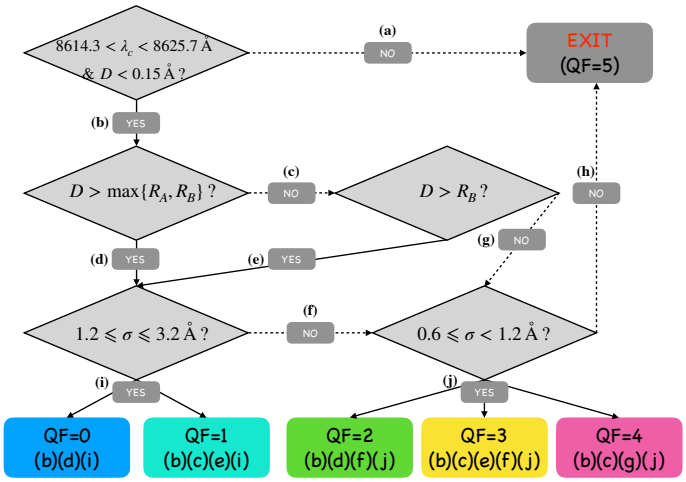

Fig. C.2. Flow chart of the different values for the DIB quality flag. See associated text in Sect. 8.9.

Table C.5. Definition of parameter flags considering potential biases due to extrapolated parameters (MatisseGauguin parametrisation, see also Table 2).

Flag name	Condition	Flag value
extrapol	gof=NaN and (Teff>9000 K or Teff<2500 K or logg>6 or logg<-1)	Filter all *except DIB if Teff>7000 K* Flag 9
	gof=NaN and 2500≤Teff≤9000 K and -1≤logg≤6 and ([M/H]<-6 dex or [M/H]>1.5 dex)	Filter [M/H],[X/Fe] Flag 4
	gof=NaN and 2500≤Teff<9000 K and -1≤logg≤6 and -6≤[M/H]≤1.5 dex and [α/Fe] out from standard by ± 0.8	Filter [X/Fe] Flag 3
	gof=NaN and 2500≤Teff≤9000 K and -1≤logg≤6 dex and -6≤[M/H]≤1.5 and [α/Fe] within ± 0.8 from standard	Flag 2
	gof ≠NaN and (Teff≥7625 or Teff≤3500 K or logg≥4.75 or logg≤0.25 or [M/H]≤-3 or [M/H]≥0.75 dex or [α/Fe] out from standard by ± 0.35)	Flag 1
	gof ≠NaN and 3500<Teff<7625 K and 0.25<logg<4.75 and -3<[M/H]<0.75 dex and [α/Fe] within ± 0.35 from standard	Flag 0

Table C.6. Same as Table C.5 but for the ANN parametrisation.

ANN extrapol	
Condition	**Value**
$T_{\rm eff}$>8320 K or $T_{\rm eff}$<3680 K or log(g)>6.0 or log(g)<-1.0 or [M/H]>1.3 dex or [M/H]<-5.3 dex or [α/Fe]>1.0 dex or [α/Fe]<-0.6 dex	Flag 9
7680<$T_{\rm eff}$≤8320 K or 3680≤$T_{\rm eff}$<4320 K or 4.9<log(g)≤6.0 or -1.0≤log(g)<0.06 or 0.6<[M/H]≤1.4 dex or -5.3≤[M/H]<-4.6 dex or 0.6<[α/Fe]≤1.0 dex or -0.5≤[α/Fe]<0.2 dex	Flag 1
4320≤$T_{\rm eff}$≤7680 K and 0.06≤log(g)≤4.9 and -4.6≤[M/H]≤0.6 dex and -0.2≤[α/Fe]≤0.6 dex	Flag 0

Table C.7. Definition of parameter flags considering RVS flux issues or emission line probability (see also Table 2).

Flag name	Condition	Flag value
nanFlux	Flux=NaN	Filter all *except DIB if Teff>7000 K* Flag 9
emission	*CU6_is_emission*	Filter all *except DIB if Teff>7000 K* Flag 9
negFlux	> 2 *wlp* with flux<0	Filter all *except DIB if Teff>7000 K* Flag 9
	1 or 2 *wlp* with flux<0	Flag 1
	flux>0	Flag 0
nullFluxErr	σTeff=0 K or σlogg=0 dex or σ[M/H]=0 dex or σ[α/Fe]=0 dex	Filter all Flag 9

Table C.8. Definition of the parameter flag considering problems in the paramerisation of KM-type giants. $F_{\rm min}$ is the minimum flux value in the corresponding RVS spectrum (see also Table 2).

Flag name	Condition	Flag value
KM-type stars	$T_{\rm eff}$<4000 K and log(g)<3.5 and (gof >-3.0 and $F_{\rm min}$ >0.22)	Flag 2 Filter [α/Fe]
	$T_{\rm eff}$<4000 K and log(g)<3.5 and [(-3.4< gof <-3.0) or (gof >-3.0 and $F_{\rm min}$ <0.22) or (gof <-3.4 and $F_{\rm min}$ >0.22)]	Flag 1 Filter [α/Fe]
	[$T_{\rm eff}$<4000 K and log(g)<3.5 and (gof <-3.4 or $F_{\rm min}$ <0.22)] or $T_{\rm eff}$>4000 or log(g)>3.5	Flag 0

Table C.9. Definition of individual abundance upper limit flags (see Table 2). Xfe_gspspec_upper is the upper confidence value of the abundance (corresponding to the 84th quantile of the Monte-Carlo distribution). σ[X/Fe] is the 84th-16th interquantile abundance uncertainty. XfeUpperLimit is the mean value of the abundance upper limit for the considered lines of the X-element in the spectrum (depending on the mean S/N in the line *wlp* and the stellar parameters). X_MAD_UpperLimit is the median absolute deviation of upper limit in the line *wlp*. Finally, the c-coefficients are reported in Table C.11.

Flag name	Condition	Flag value
XUpLim	vbroadT≥2 or vbroadG≥2 or vbroadM≥2 or σ[X/Fe] = 0 or (Xfe_gspspec_upper - Xfe_gspspec) = 0 or Teff≤c1 or Teff≥c2 or logg≤c3 or logg≥c4 or ((2 - XfeUpperLimit) / σ[X/Fe])≤c5 or (S/N≤c6 and gof≥c7) or (Xfe_gspspec + [M/H])≤c8	Flag 9 Filter [X/Fe]
	vbroadT<2 and vbroadG<2 and vbroadM<2 and σ[X/Fe] != 0 and (Xfe_gspspec_upper - Xfe_gspspec) != 0 and c1<Teff<c2 and c3<logg<c4 and ((2 - XfeUpperLimit) / σ[X/Fe])>c5 and (S/N>c6 or gof<c7) and (Xfe_gspspec + [M/H])<c8 and ((Xfe_gspspec - XfeUpperLimit) / (1.48·X_MAD_UpperLimit))<1.5	Flag 2
	vbroadT<2 and vbroadG<2 and vbroadM<2 and σ[X/Fe] != 0 and (Xfe_gspspec_upper- Xfe_gspspec) != 0 and c1<Teff<c2 and c3<logg<c4 and ((2 - XfeUpperLimit) / σ[X/Fe])>c5 and (S/N>c6 or gof<c7) and (Xfe_gspspec+[M/H])<c8 and 1.5≤((Xfe_gspspec - XfeUpperLimit) / (1.48·X_MAD_UpperLimit))<2.5	Flag 1
	vbroadT<2 and vbroadG<2 and vbroadM<2 and σ[X/Fe] != 0 and (Xfe_gspspec_upper - Xfe_gspspec) != 0 and c1<Teff<c2 and c3<logg<c4 and ((2 - XfeUpperLimit) / σ[X/Fe])>c5 and (S/N>c6 or gof<c7) and (Xfe_gspspec + [M/H])<c8 and ((Xfe_gspspec - XfeUpperLimit) / (1.48·X_MAD_UpperLimit))≥2.5	Flag 0

Table C.10. Definition of individual abundance uncertainty flags (see Table 2). Xfe_gspspec_upper is the upper confidence value of the abundance (corresponding to the 84th quantile of the Monte-Carlo distribution). σ[X/Fe] is the 84th-16th interquantile abundance uncertainty. XfeUpperLimit is the mean value of the abundance upper limit for the considered lines of the X-element in the spectrum (depending on the mean S/N in the line *wlp* and the stellar parameters). Finally, the c-coefficients are reported in Table C.11.

Flag name	Condition	Flag value
XUncer	vbroadT≥2 or vbroadG≥2 or vbroadM≥2 or σ[X/Fe]=0 or (Xfe_gspspec_upper - Xfe_gspspec) = 0 or Teff≤c1 or Teff≥c2 or logg≤c3 or logg≥c4 or ((2-XfeUpperLimit) / σ[X/Fe])≤c5 or (S/N≤c6 and gof≥c7) or (Xfe_gspspec + [M/H])≤c8	Flag 9 Filter [X/Fe]
	vbroadT<2 and vbroadG<2 and vbroadM<2 and σ[X/Fe] != 0 and (Xfe_gspspec_upper - Xfe_gspspec) != 0 and c1<Teff<c2 and c3<logg<c4 and c5<((2 - XfeUpperLimit) / σ[X/Fe])<7 and (S/N>c6 or gof<c7) and (Xfe_gspspec + [M/H])<c8	Flag 2
	vbroadT<2 and vbroadG<2 and vbroadM<2 and σ[X/Fe] != 0 and (Xfe_gspspec_upper - Xfe_gspspec) != 0 and c1<Teff<c2 and c3<logg<c4 and 7 ≤ ((2 - XfeUpperLimit) / σ[X/Fe]) < 10 and (S/N>c6 or gof<c7) and (Xfe_gspspec + [M/H])<c8	Flag 1
	vbroadT<2 and vbroadG<2 and vbroadM<2 and σ[X/Fe] != 0 and (Xfe_gspspec_upper - Xfe_gspspec) != 0 and c1<Teff<c2 and c3<logg<c4 and ((2 - XfeUpperLimit) / σ[X/Fe]) ≥ 10 and (S/N>c6 or gof<c7) and (Xfe_gspspec + [M/H])<c8	Flag 0

Table C.11. Coefficients for individual chemical abundance filtering (see [X/Fe] upperLimit flag and σ[X/Fe] quality flag in Table C.9 and C.10, respectively).

Chemical abundance	c1	c2	c3	c4	c5	c6	c7	c8
[N/Fe]	4200	8000	0.0	5.5	4.5	100	-3.6	99
[Mg/Fe]	3500	8000	-1.0	5.5	5.5	80	-3.5	99
[Si/Fe]	4000	8000	-1.0	5.5	6.0	110	-3.8	99
[S/Fe]	5500	8000	3.0	5.5	5.0	120	-3.7	99
[Ca/Fe]	3500	8000	-1.0	5.5	10.0	60	-3.2	99
[Ti/Fe]	4000	6500	-1.0	5.5	6.0	110	-3.65	99
[Cr/Fe]	3500	6000	-1.0	5.5	6.0	1000	-3.65	1.5
[Fe I/M]	3500	8000	-1.0	5.5	5.0	1000	-3.4	1.5
[Fe II/M]	5700	8000	3.5	5.5	5.0	70	-3.5	1.5
[Ni/Fe]	4000	6500	-1.0	5.5	6.0	100	-3.6	1.5
[Zr/Fe]	3500	8000	-1.0	5.5	1.0	100	-3.4	99
[Ce/Fe]	3500	8000	-1.0	5.5	5.0	100	-3.5	99
[Nd/Fe]	3500	5500	-1.0	5.5	2.0	100	-3.5	99

Table C.12. Definition of the quality flag of the CN differential EW with respect to the solar C and N abundances.

Flag name	Condition	Flag value
DeltaCNq	vbroadT≥1 or vbroadG≥1 or vbroadM≥1 or CN_EW_err = 0 or S/N ≤ 80 or gof≥-3.5 or $T_{\rm eff}$≥4800 K or log(g)≥3.8 or |CN_p1 - 849.037|≥0.05 or CN_p2≥0.25	Flag 9 Filter CN
	vbroadT<1 and vbroadG<1 and vbroadM<1 and CN_EW_err != 0 and S/N > 80 and gof <-3.5 and $T_{\rm eff}$<4800 K and log(g)<3.8 and |CN_p1 - 849.037|<0.05 and CN_p2<0.25	Flag 0

Table C.13. Definition of the quality flag for the DIB parameterisation. See Sect. 8.9 for the definition of *Ra* and *Rb*.

Flag name	Condition	Flag value
DIBq	S/N≤70 or Vrad_err > 5 km.s^{-1} or $T_{\rm eff}$<3 500 K or $T_{\rm eff}$>10^5 K or Σ_i RVS_Flux$_i$ < 0 or p$_0$ < 3/(S/N)	Flag 9 Filter DIB
	p_1 < 861.66 nm or p_1 > 862.81 nm or p_0 > 0.015 nm	Flag 5
	861.66 nm < p_1 < 862.81 nm and p_0 < R_b and 0.6 < p_2 < 1.2	Flag 4
	861.66 nm < p_1 < 862.81 nm and p_0>R_b and 0.6<p_2<1.2	Flag 3
	861.66 nm < p_1 < 862.81 nm and p_0 > $max(R_a, R_b)$ and 0.6<p_2<1.2	Flag 2
	861.66 nm < p_1 < 862.81 nm and p_0 > R_b and 1.2<p_2<3.2	Flag 1
	861.66 nm < p_1 < 862.81 nm and p_0 > $max(R_a, R_b)$ and 1.2<p_2<3.2	Flag 0

Appendix D: Bias comparisons per survey for MatisseGauguin parameters

Here, we perform a similar analysis to that shown in Sect. 9.1.1, but we investigate how the individual surveys compare with *GSP-Spec*. First of all, Figure D.1 presents a cumulative histogram of the RVS spectra S/N for the selected comparison samples between *GSP-Spec* MatisseGauguin and RAVE-DR6, GALAH-DR3, and APOGEE-DR17. As expected from the selection functions of the different ground-based surveys, RAVE-DR6 targets have RVS spectra with higher S/N values than GALAH-DR3 or APOGEE-DR17.

Figure D.2 is the equivalent to Fig. 11, showing only the 99 and 66 percent contour lines for RAVE-DR6 (in black), GALAH-DR3 (in red), and APOGEE-DR17 in blue. Table D.1

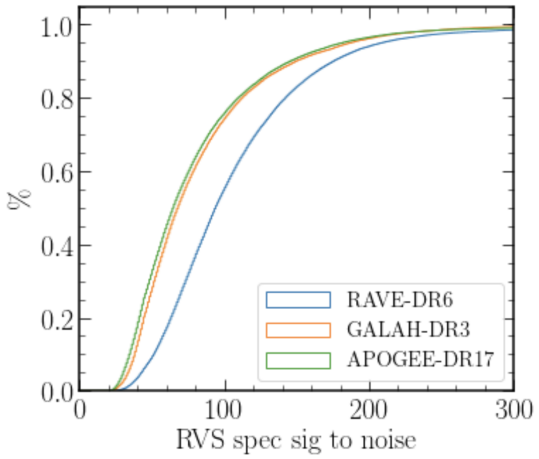

Fig. D.1. Cumulative histogram of RVS S/N for the selected comparison sample between *GSP-Spec* MatisseGauguin and three ground-based surveys: RAVE-DR6, GALAH-DR3, APOGEE-DR17. Table D.1 provides the median values and standard deviation per survey.

quantifies the comparisons, by showing the median offset (*GSP-Spec* – reference) as well as the robust sigma before and after the calibration for each survey. One can see that trends are similar no matter the reference catalogue, and that the biases are significantly decreased when using the calibrated values. It is important to note here that RVS-RAVE targets benefit from a higher S/N with respect to those of RVS-GALAH and RVS-APOGEE.

Finally, we investigated how *GSP-Spec* MatisseGauguin and the literature uncertainties compare to the observed parameter differences. To this purpose, Figure D.3 shows, in blue, the histograms of the $T_{\rm eff}$ (left column), log(g) (middle column), and [M/H] (right column) differences with respect to RAVE-DR6 (upper row), GALAH-DR3 (middle row), and APOGEE-DR17 (lower row). *GSP-Spec* MatisseGauguin log(g) and [M/H] values are calibrated. These parameter differences are normalised by the total uncertainty (defined as the quadratic sum of the *GSP-Spec* and the survey's uncertainties). The dotted histograms show the same distributions inflating the reported uncertainties by a factor of 4. Additionally, the red curves show a normal distribution of unit dispersion and zero mean. An unbiased parameter estimation with correct uncertainties should follow this distribution. Regarding the effective temperature, the reported uncertainties from both *GSP-Spec* and the literature seem to correspond to the observed differences (with some uncertainty overestimation for the RVS-GALAH sample). Regarding log(g), the situation differs from one survey to another. While the agreement between *GSP-Spec* MatisseGauguin and GALAH is good and the reported uncertainties appear overestimated again, the comparison with RAVE and APOGEE suggests that the reported uncertainties are underestimated by a factor of 2 or 3 (the factor 4 is excluded by the normal distribution). Finally, the right column histograms show that [M/H] uncertainties are coherent with the observed differences between *GSP-Spec* and RAVE. However, [M/H] uncertainties from *GSP-Spec* or the GALAH/APOGEE reference or both seem underestimated by about a factor of 4. While in these examples, we only illustrate the impact of artificially inflating *GSP-Spec* uncertainties (through the dotted histograms), it cannot be excluded that the disagreement with respect to the normal distribution is caused by an underestimation of the uncertainties reported by the literature, as possibly suggested by the variety of situations that exist, for the same atmospheric parameter, when comparing to different surveys.

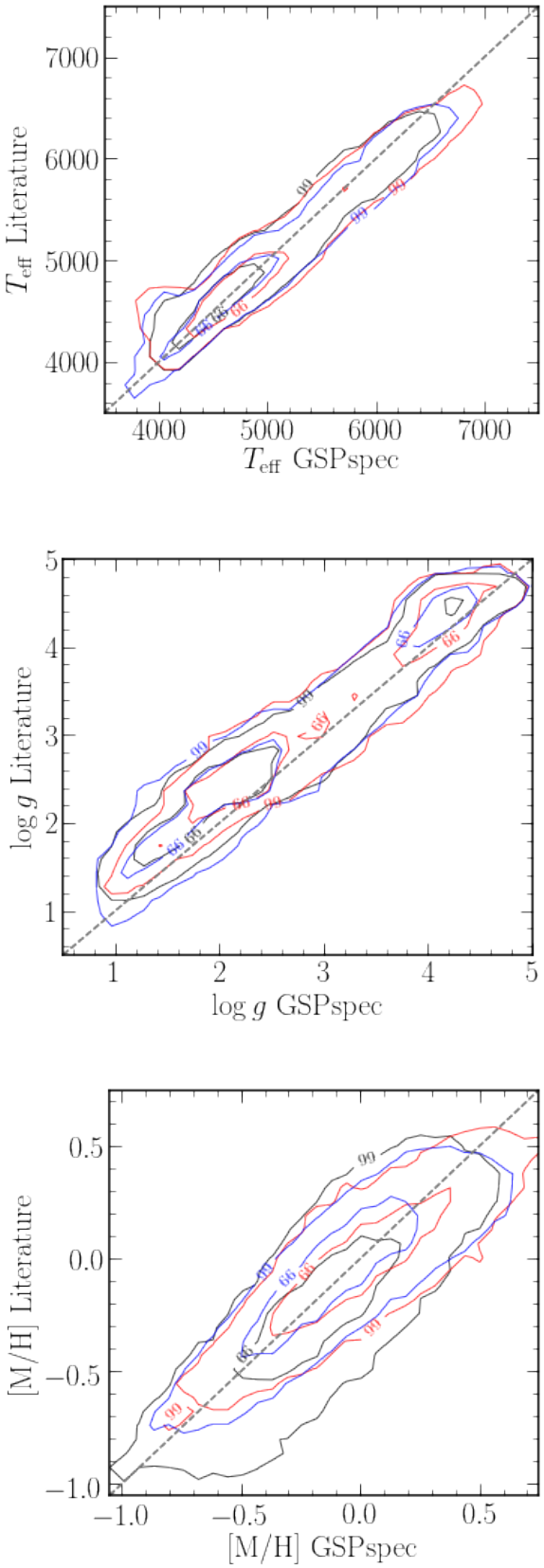

Fig. D.2. Similar to Fig. 11 but showing only the contour lines of the 99th and 66th percentiles for RAVE-DR6 (black), GALAH-DR3 (red), and APOGEE-DR17 (blue).

This analysis illustrates the complexity of comparing parametrisation results from different sources, each of them with its own uncertainty definitions, methodological and theoretical trends, and underlying selection functions. Once again, the importance of using a homogeneous catalogue for scientific purposes rather than a compilation of different sources (even after re-calibrations) is highlighted.

Table D.1. Median offsets and robust sigma between *GSP-Spec* and individual surveys.

	$T_{\rm eff}$	$\log(g)$	[M/H]	$\log(g)_{\rm calibrated}$	[M/H]$_{\rm calibrated}$	RVS S/N
RAVE-DR6	(-12; 93)	(-0.28; 0.19)	(-0.05; 0.11)	(-0.003; 0.18)	(-0.05; 0.09)	(94; 64)
GALAH-DR3	(20;87)	(-0.26; 0.21)	(0.01; 0.10)	(0.003; 0.18)	(-0.001; 0.10)	(68; 53)
APOGEE-DR17	(-32; 86)	(-0.32; 0.17)	(0.04; 0.12)	(-0.005; 0.15)	(0.06; 0.12)	(65; 80)

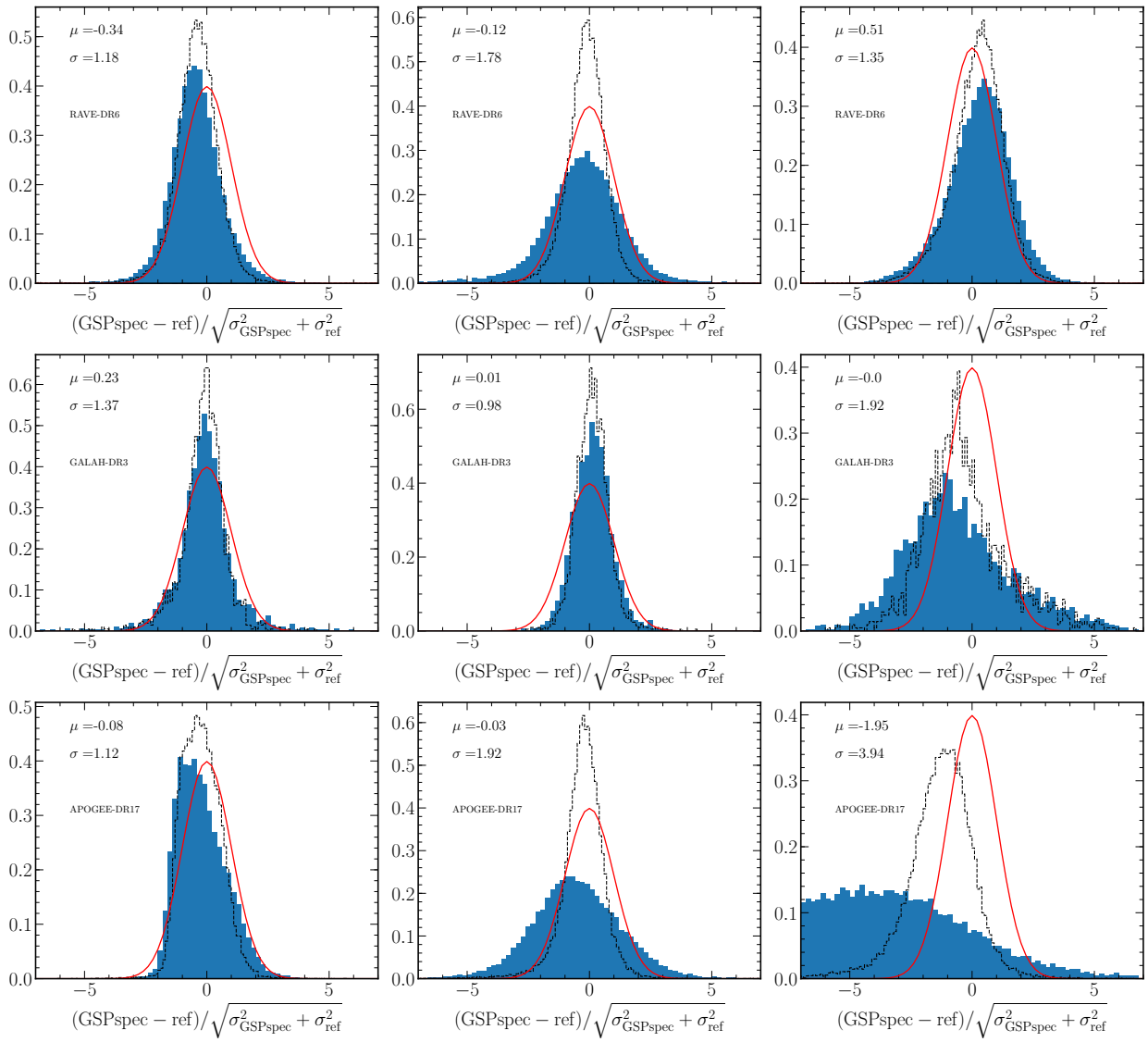

Fig. D.3. Distributions of parameter differences, normalised with respect to the reported *GSP-Spec* and literature uncertainties. From left to right: $T_{\rm eff}$, $\log(g)$, and [M/H] differences. From up to bottom: Differences with respect to RAVE-DR6, GALAH-DR3, and APOGEE-DR17. Dotted histograms correspond to the same distributions inflating the uncertainties (*GSP-Spec* and literature) by a factor of 4. The red curve shows a normal distribution of unit dispersion and zero mean. An unbiased parameter estimation with correct uncertainties should follow this distribution.

Appendix E: Illustration of polynomial corrections for MatisseGauguin chemical abundances and quantification of uncertainties

Figures E.1 and E.2 illustrate the calibrations for individual chemical abundances and the comparison with literature data presented in Sect. 9.1.2. In addition, the uncertainties in the polynomial coefficients p_1, p_2, p_3, and p_4 provided in Table 4 are presented in Table E.1.

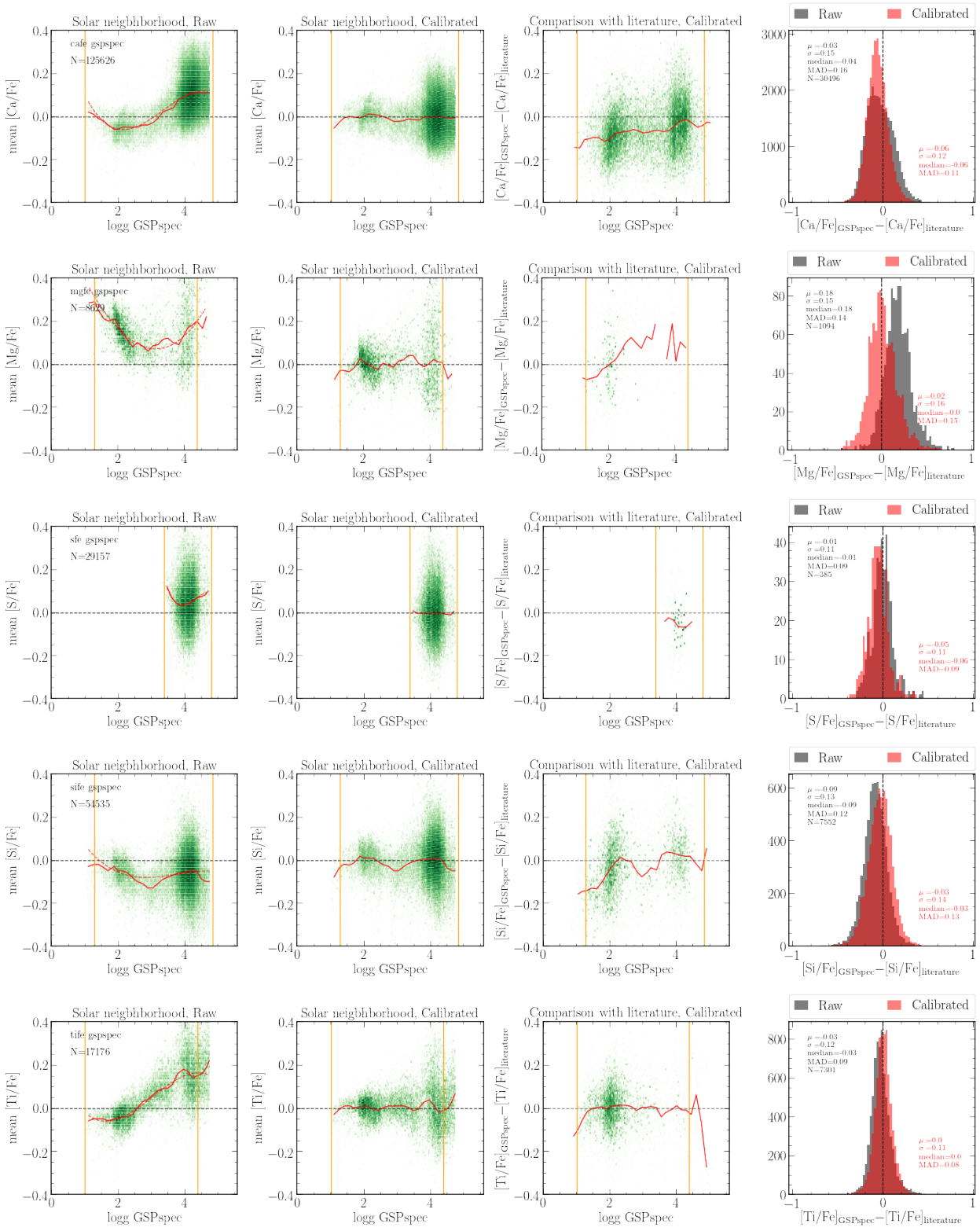

Fig. E.1. Same as Fig. 14, but for individual α-elements.

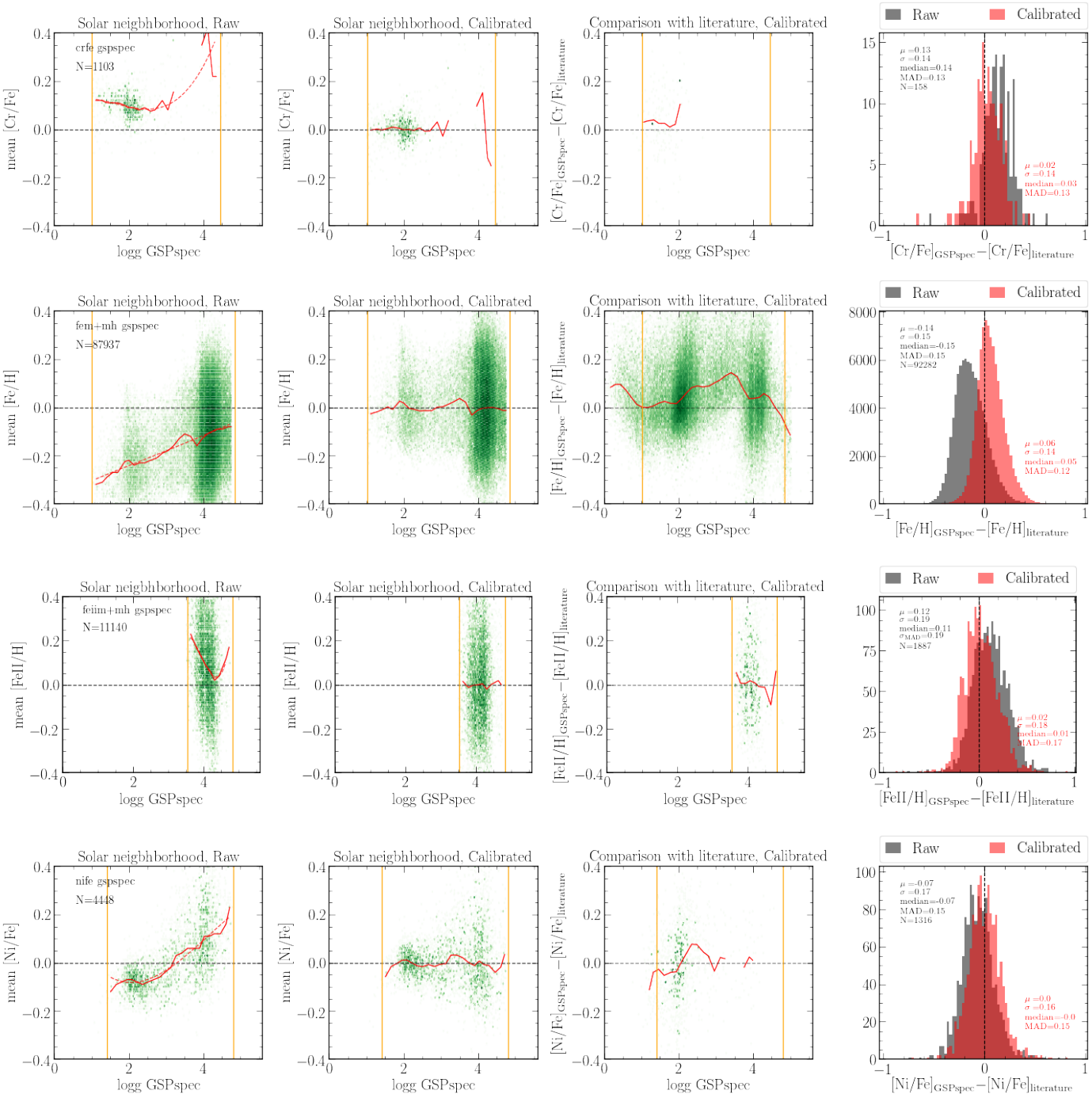

Fig. E.2. Same as Fig. 14, but for individual iron-peak elements.

Table E.1. Uncertainties on the polynomial coefficients of Table 4.

Element	δp_0	δp_1	δp_2	δp_3	δp_4	*extrapol* flag
	As a function of log(g)					
[α/Fe]	0.0965	0.0960	0.0302	0.0031	0.0000	0
[Ca/Fe]	0.0750	0.0747	0.0236	0.0024	0.0000	0
[Mg/Fe]	0.2002	0.2252	0.0819	0.0095	0.0000	0
[S/Fe]	6.5357	4.7804	1.1639	0.0943	0.0000	0
[Si/Fe]	0.1491	0.1562	0.0522	0.0056	0.0000	0
[Ti/Fe]	0.0729	0.0807	0.0286	0.0032	0.0000	0
[Cr/Fe]	0.0951	0.1310	0.0571	0.0077	0.0000	0
[Fe I/H]	0.1254	0.1260	0.0401	0.0041	0.0000	0
[Fe II/H]	13.9985	10.1731	2.4608	0.1981	0.0000	0
[Ni/Fe]	0.1829	0.1979	0.0692	0.0078	0.0000	0
[N/Fe]	0.0580	0.0716	0.0283	0.0035	0.0000	0
[α/Fe]	0.0646	0.0971	0.0524	0.0119	0.0010	≤1
[Ca/Fe]	0.1000	0.1419	0.0726	0.0158	0.0012	≤1
	As a function of t=$T_{\rm eff}$/5750					
[α/Fe]	0.5852	1.8825	2.0028	0.7049	0.0000	≤1
[Ca/Fe]	0.7270	2.3284	2.4674	0.8655	0.0000	≤1
[S/Fe]	0.0323	0.0300	0.0000	0.0000	0.0000	≤1

Appendix F: Validation of ANN biases and uncertainties as a function of S/N

As explained in Sect. 7, the ANN algorithm is trained with noisy spectra to optimise the parametrisation in different S/N regimes. For this reason, it is important to validate the correct behaviour of internal and external errors as a function of S/N.

To study the internal biases and uncertainties, a parametrisation test with a random sample of 10 000 synthetic spectra in the three S/N regimes listed in Table 1 was performed. First of all, we studied the global behaviour of the bias as a function of S/N and a possible dependency of the bias on the parameters themselves by fitting the obtained parameter X^{ANN} as a function of the true parameter X^{Syn} (Fig. F.1). To model this behaviour, we use three different functions: a simple straight line, a parabola, and a piecewise first-order polynomial function (two, three, and five degrees of freedom, respectively) selecting as the best function the one with the smallest Bayesian information criterion (BIC). This process is repeated for each S/N.

In addition, for each S/N, the internal uncertainty (σ_{inter}) on each parameter was estimated from the standard deviation of the distribution $X^{ANN} - X^{Syn}$. The internal uncertainty trends with S/ N are shown in Figure F.2 together with the function that best fits these points. To find this best-fit function, two possible functional relationships were considered: simple parabolic and an inverse square root of the S/N, selecting once again the function with the minimum BIC. It is worth noting that the preferred function is the inverse square root function in all S/N bins, confirming the consistency of the estimations and leading to the following equations:

$$\sigma_{inter\_Teff} = -505 + 4763/\sqrt{S/N}, \quad \text{(F.1)}$$

$$\sigma_{inter\_logg} = -0.9 + 8/\sqrt{S/N}, \quad \text{(F.2)}$$

$$\sigma_{inter\_[M/H]} = -0.6 + 5/\sqrt{S/N}, \quad \text{(F.3)}$$

$$\sigma_{inter\_[\alpha/Fe]} = -0.6 + 5/\sqrt{S/N}. \quad \text{(F.4)}$$

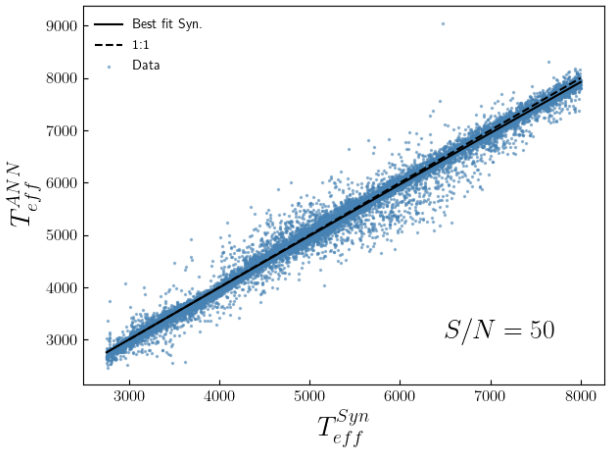

Fig. F.1. Illustration of the ANN tests with synthetic spectra to evaluate internal biases and uncertainties, for S/N$_{ANN}$ =50. The estimated $T_{\rm eff}{}^{ANN}$ as a function of the true parameter $T_{\rm eff}{}^{Syn}$ is shown, including the polynomial fit modelling the observed behaviour. Similar analyses were performed for log(g), [M/H], and [α/Fe].

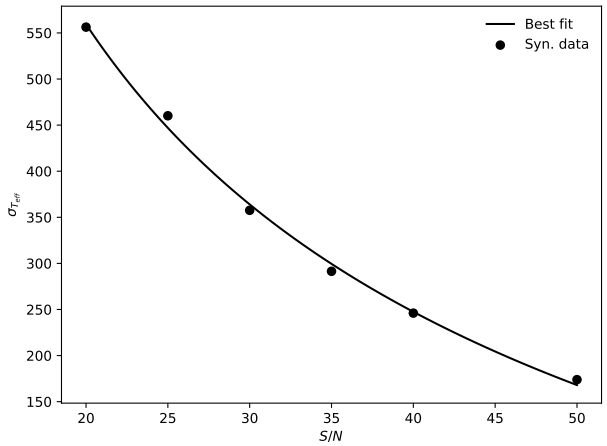

Fig. F.2. Illustration of the estimated trends on the internal ANN T_{eff} uncertainty with S/N. The best fit to this trend is also shown. A similar analysis was performed for log(g), [M/H], and [α/Fe].

Table F.1 summarises the estimated internal biases and uncertainties as a function of S/N. As expected, internal biases are negligible.

Finally, to complete the previous validation of the trend of the ANN estimates with S/N, the differences with respect to the literature (see Sect. 9.2) were examined. As a significant proportion of results from the three reference surveys have an important S/N dependence, with the lower resolution RAVE survey dominating for brighter sources in the high-S/N regime, we decided to validate the uncertainty behaviour with S/N with APOGEE DR16 and GALAH DR3 exclusively[20]. Figure F.3 illustrates the distribution of $T_{\rm eff}$ differences with respect to the literature for the five S/N regimes of the ANN training. Similar analyses were performed for the other three atmospheric parameters and the estimated biases and mean absolute deviations are reported in Table F.2. The expected increase in the spread for lower S/N regimes can be seen, validating the S/N optimisation of the ANN algorithm.

[20] These two surveys, as expected from their higher wavelength coverage and resolution, also show a better agreement with ANN parameters for sources with S/N>50.

Table F.1. ANN internal biases and uncertainties (from the mean absolute deviation) in the different S/N regimes considered for the ANN training.

S/N		$T_{\rm eff}$	log(g)	[M/H]	[α/Fe]
50	Bias	-19 K	-0.02 dex	0.03 dex	-0.01 dex
	MAD	102 K	0.16 dex	0.13 dex	0.06 dex
40	Bias	30 K	-0.07 dex	-0.01 dex	0.02 dex
	MAD	149 K	0.25 dex	0.18 dex	0.09 dex
35	Bias	39 K	-0.01 dex	0.07 dex	0.02 dex
	MAD	179 K	0.31 dex	0.21 dex	0.11 dex
30	Bias	-22 K	-0.01 dex	-0.05 dex	0.01 dex
	MAD	233 K	0.41 dex	0.28 dex	0.13 dex
25	Bias	-2 K	-0.01 dex	0.03 dex	0.01 dex
	MAD	318 K	0.56 dex	0.38 dex	0.16 dex

Table F.2. ANN biases and mean absolute deviations with respect to the literature, in the different S/N regimes considered for the ANN training.

S/N		$T_{\rm eff}$	log(g)	[M/H]	[α/Fe]
50	Bias	-162 K	-0.13 dex	-0.29 dex	0.07 dex
	MAD	155 K	0.21 dex	0.15 dex	0.05 dex
40	Bias	-89 K	-0.10 dex	-0.26 dex	0.10 dex
	MAD	139 K	0.29 dex	0.13 dex	0.07 dex
35	Bias	-38 K	0.005 dex	-0.25 dex	0.12 dex
	MAD	148 K	0.32 dex	0.15 dex	0.08 dex
30	Bias	-6 K	-0.04 dex	-0.32 dex	0.11 dex
	MAD	192 K	0.42 dex	0.19 dex	0.11 dex
25	Bias	-98 K	-0.02 dex	-0.43 dex	0.09 dex
	MAD	253 K	0.47 dex	0.25 dex	0.12 dex

Table F.3. Polynomial coefficients for the $T_{\rm eff}$ calibration at different S/N$_{ANN}$ values.

	S/N_{ANN}	p_0	p_1	p_2	p_3
$T_{\rm eff}$	30	-834	3.13E-1	-2.53E-5	
	35	-1344	4.95E-1	-4.26E-5	
	40	3182	-2.34	5.38E-4	-3.84E-8
	50	12816	-8.1	1.65E-3	-1.07E-7

After the analysis of the uncertainties, we realised that there is a direct relation between $T_{\rm eff}$ and S/N and so we decided to propose different calibrations depending on the S/N ranges defined in Table 1. Furthermore, we observed that the number of stars with $T_{\rm eff}$ > 6000 K in the literature is statistically insignificant, and so the calibration beyond this limit should not be applied. For log(g), [M/H], and [α/Fe], although there is an intrinsic relation with S/N, the global calibration proved to be the best solution. We provide the calibration of $T_{\rm eff}$ for S/N$_{ANN}$ ~50 in Section 9.2 and we give the polynomial coefficients for lower S/N in Table F.3.

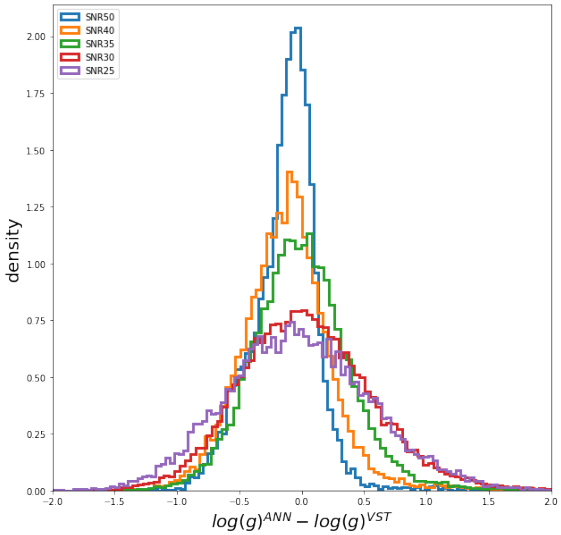

Fig. F.3. Error distributions for ANN estimations with respect to the literature (Validation Source Table - VST).

Appendix G: Query examples from the Gaia Archive

G.1. MatisseGauguin parameters from the AstrophysicalParameters table

```
SELECT source_id
FROM user_dr3int6.astrophysical_parameters
WHERE ((teff_gspspec>=3800) OR (logg_gspspec>=3.5))
    AND ((teff_gspspec>=4150) OR (logg_gspspec>=3.6)
    OR (logg_gspspec<=2.4))
```

Listing 1. ADQL query example with simple cuts in the limiting parameters.

```
SELECT source_id
FROM user_dr3int6.astrophysical_parameters
WHERE (teff_gspspec>3500) AND (logg_gspspec>0) AND
    (logg_gspspec<5) AND
    ((teff_gspspec_upper-teff_gspspec_lower)<750)
    AND ((logg_gspspec_upper-logg_gspspec_lower)<1.)
    AND ((mh_gspspec_upper-mh_gspspec_lower)<.5) AND
    (teff_gspspec>=3800 OR logg_gspspec<=3.5) AND
    (teff_gspspec>=4150 OR logg_gspspec<=2.4 OR
    logg_gspspec>=3.6 ) AND ((flags_gspspec LIKE
    "____________0%") OR (flags_gspspec LIKE
    "____________1%")) AND ((flags_gspspec LIKE
    "0%") OR (flags_gspspec LIKE "1%")) AND
    ((flags_gspspec LIKE "_0%") OR (flags_gspspec
    LIKE "_1%")) AND ((flags_gspspec LIKE "__0%") OR
    (flags_gspspec LIKE "__1%")) AND ((flags_gspspec
    LIKE "___0%") OR (flags_gspspec LIKE "___1%"))
    AND ((flags_gspspec LIKE "____0%") OR
    (flags_gspspec LIKE "____1%")) AND
    ((flags_gspspec LIKE "_____0%") OR
    (flags_gspspec LIKE "_____1%")) AND
    ((flags_gspspec LIKE "______0%") OR
    (flags_gspspec LIKE "______1%") OR
    (flags_gspspec LIKE "______2%") OR
    (flags_gspspec LIKE "______3%")) AND
    ((flags_gspspec LIKE "_______0%") OR
    (flags_gspspec LIKE "_______1%") OR
    (flags_gspspec LIKE "_______2%"))
```

Listing 2. ADQL query example including conditions on the parameter flags (c.f. Table 2).

G.2. ANN parameters from the AstrophysicalParametersSupp table

```
SELECT source_id, teff_gspspec_ann, logg_gspspec_ann,
    mh_gspspec_ann, alphafe_gspspec_ann,
    flags_gspspec_ann
FROM user_dr3int6.astrophysical_parameters_supp
WHERE TO_BIGINT(flags_gspspec_ann) < 10000
```

Listing 3. Best quality sources, no S/N dependency (~1.3 M sources).

```
SELECT ann.source_id, teff_gspspec_ann,
    logg_gspspec_ann, mh_gspspec_ann,
    alphafe_gspspec_ann, flags_gspspec_ann,
    rv_expected_sig_to_noise
FROM user_dr3int6.gaia_source as gaia RIGHT JOIN
   (
   SELECT source_id, teff_gspspec_ann,
       logg_gspspec_ann, mh_gspspec_ann,
       alphafe_gspspec_ann, flags_gspspec_ann
   FROM user_dr3int6.astrophysical_parameters_supp
   WHERE TO_BIGINT(flags_gspspec_ann) < 10000
   ) as ann USING(source_id)
WHERE rv_expected_sig_to_noise > 108
```

Listing 4. Best quality sources with S/N > 108 (S/N_{ANN} 50) (~275 k sources).

Appendix H: Acknowledgements

(*Funding*) The *Gaia* mission and data processing have financially been supported by, in alphabetical order by country:
– the Algerian Centre de Recherche en Astronomie, Astrophysique et Géophysique of Bouzareah Observatory;
– the Austrian Fonds zur Förderung der wissenschaftlichen Forschung (FWF) Hertha Firnberg Programme through grants T359, P20046, and P23737;
– the BELgian federal Science Policy Office (BELSPO) through various PROgramme de Développement d'Expériences scientifiques (PRODEX) grants, the Research Foundation Flanders (Fonds Wetenschappelijk Onderzoek) through grant VS.091.16N, the Fonds de la Recherche Scientifique (FNRS), and the Research Council of Katholieke Universiteit (KU) Leuven through grant C16/18/005 (Pushing AsteRoseismology to the next level with TESS, GaiA, and the Sloan DIgital Sky SurvEy – PARADISE);
– the Brazil-France exchange programmes Fundação de Amparo à Pesquisa do Estado de São Paulo (FAPESP) and Coordenação de Aperfeicoamento de Pessoal de Nível Superior (CAPES) - Comité Français d'Evaluation de la Coopération Universitaire et Scientifique avec le Brésil (COFECUB);
– the Chilean Agencia Nacional de Investigación y Desarrollo (ANID) through Fondo Nacional de Desarrollo Científico y Tecnológico (FONDECYT) Regular Project 1210992 (L. Chemin);
– the National Natural Science Foundation of China (NSFC) through grants 11573054, 11703065, and 12173069, the China Scholarship Council through grant 201806040200, and the Natural Science Foundation of Shanghai through grant 21ZR1474100;
– the Tenure Track Pilot Programme of the Croatian Science Foundation and the École Polytechnique Fédérale de Lausanne and the project TTP-2018-07-1171 'Mining the Variable Sky', with the funds of the Croatian-Swiss Research Programme;
– the Czech-Republic Ministry of Education, Youth, and Sports through grant LG 15010 and INTER-EXCELLENCE grant LTAUSA18093, and the Czech Space Office through ESA PECS contract 98058;
– the Danish Ministry of Science;
– the Estonian Ministry of Education and Research through grant IUT40-1;
– the European Commission's Sixth Framework Programme through the European Leadership in Space Astrometry (ELSA) Marie Curie Research Training Network (MRTN-CT-2006-033481), through Marie Curie project PIOF-GA-2009-255267 (Space AsteroSeismology & RR Lyrae stars, SAS-RRL), and through a Marie Curie Transfer-of-Knowledge (ToK) fellowship (MTKD-CT-2004-014188); the European Commission's Seventh Framework Programme through grant FP7-606740 (FP7-SPACE-2013-1) for the *Gaia* European Network for Improved data User Services (GENIUS) and through grant 264895 for the *Gaia* Research for European Astronomy Training (GREAT-ITN) network;
– the European Cooperation in Science and Technology (COST) through COST Action CA18104 'Revealing the Milky Way with *Gaia* (MW-Gaia)';
– the European Research Council (ERC) through grants 320360, 647208, and 834148 and through the European Union's Horizon 2020 research and innovation and excellent science programmes through Marie Skłodowska-Curie grant 745617 (Our Galaxy at full HD – Gal-HD) and 895174 (The build-up and fate of self-gravitating systems in the Universe) as well as grants 687378 (Small Bodies: Near and Far), 682115 (Using the Magellanic Clouds to Understand the Interaction of Galaxies), 695099 (A sub-percent distance scale from binaries and Cepheids – CepBin), 716155 (Structured ACCREtion Disks – SACCRED), 951549 (Sub-percent calibration of the extragalactic distance scale in the era of big surveys – UniverScale), and 101004214 (Innovative Scientific Data Exploration and Exploitation Applications for Space Sciences – EXPLORE);
– the European Science Foundation (ESF), in the framework of the *Gaia* Research for European Astronomy Training Research Network Programme (GREAT-ESF);
– the European Space Agency (ESA) in the framework of the *Gaia* project, through the Plan for European Cooperating States (PECS) programme through contracts C98090 and 4000106398/12/NL/KML for Hungary, through contract 4000115263/15/NL/IB for Germany, and through PROgramme de Développement d'Expériences scientifiques (PRODEX) grant 4000127986 for Slovenia;
– the Academy of Finland through grants 299543, 307157, 325805, 328654, 336546, and 345115 and the Magnus Ehrnrooth Foundation;
– the French Centre National d'Études Spatiales (CNES), the Agence Nationale de la Recherche (ANR) through grant ANR-10-IDEX-0001-02 for the 'Investissements d'avenir' programme, through grant ANR-15-CE31-0007 for project 'Modelling the Milky Way in the *Gaia* era' (MOD4Gaia), through grant ANR-14-CE33-0014-01 for project 'The Milky Way disc formation in the *Gaia* era' (ARCHEOGAL), through grant ANR-15-CE31-0012-01 for project 'Unlocking the potential of Cepheids as primary distance calibrators' (UnlockCepheids), through grant ANR-19-CE31-0017 for project 'Secular evolution of galaxies' (SEGAL), and through grant ANR-18-CE31-0006 for project 'Galactic Dark Matter' (GaDaMa), the Centre National de la Recherche Scientifique (CNRS) and its SNO *Gaia* of the Institut des Sciences de l'Univers (INSU), its Programmes Nationaux: Cosmologie et Galaxies (PNCG), Gravitation Références Astronomie Métrologie (PNGRAM), Planétologie (PNP), Physique et Chimie du

Milieu Interstellaire (PCMI), and Physique Stellaire (PNPS), the 'Action Fédératrice *Gaia* ' of the Observatoire de Paris, the Région de Franche-Comté, the Institut National Polytechnique (INP) and the Institut National de Physique nucléaire et de Physique des Particules (IN2P3) co-funded by CNES;
– the German Aerospace Agency (Deutsches Zentrum für Luft- und Raumfahrt e.V., DLR) through grants 50QG0501, 50QG0601, 50QG0602, 50QG0701, 50QG0901, 50QG1001, 50QG1101, 50QG1401, 50QG1402, 50QG1403, 50QG1404, 50QG1904, 50QG2101, 50QG2102, and 50QG2202, and the Centre for Information Services and High Performance Computing (ZIH) at the Technische Universität Dresden for generous allocations of computer time;
– the Hungarian Academy of Sciences through the Lendület Programme grants LP2014-17 and LP2018-7 and the Hungarian National Research, Development, and Innovation Office (NKFIH) through grant KKP-137523 ('SeismoLab');
– the Science Foundation Ireland (SFI) through a Royal Society - SFI University Research Fellowship (M. Fraser);
– the Israel Ministry of Science and Technology through grant 3-18143 and the Tel Aviv University Center for Artificial Intelligence and Data Science (TAD) through a grant;
– the Agenzia Spaziale Italiana (ASI) through contracts I/037/08/0, I/058/10/0, 2014-025-R.0, 2014-025-R.1.2015, and 2018-24-HH.0 to the Italian Istituto Nazionale di Astrofisica (INAF), contract 2014-049-R.0/1/2 to INAF for the Space Science Data Centre (SSDC, formerly known as the ASI Science Data Center, ASDC), contracts I/008/10/0, 2013/030/I.0, 2013-030-I.0.1-2015, and 2016-17-I.0 to the Aerospace Logistics Technology Engineering Company (ALTEC S.p.A.), INAF, and the Italian Ministry of Education, University, and Research (Ministero dell'Istruzione, dell'Università e della Ricerca) through the Premiale project 'MIning The Cosmos Big Data and Innovative Italian Technology for Frontier Astrophysics and Cosmology' (MITiC);
– the Netherlands Organisation for Scientific Research (NWO) through grant NWO-M-614.061.414, through a VICI grant (A. Helmi), and through a Spinoza prize (A. Helmi), and the Netherlands Research School for Astronomy (NOVA);
– the Polish National Science Centre through HARMONIA grant 2018/30/M/ST9/00311 and DAINA grant 2017/27/L/ST9/03221 and the Ministry of Science and Higher Education (MNiSW) through grant DIR/WK/2018/12;
– the Portuguese Fundação para a Ciência e a Tecnologia (FCT) through national funds, grants SFRH/BD/128840/2017 and PTDC/FIS-AST/30389/2017, and work contract DL 57/2016/CP1364/CT0006, the Fundo Europeu de Desenvolvimento Regional (FEDER) through grant POCI-01-0145-FEDER-030389 and its Programa Operacional Competitividade e Internacionalização (COMPETE2020) through grants UIDB/04434/2020 and UIDP/04434/2020, and the Strategic Programme UIDB/00099/2020 for the Centro de Astrofísica e Gravitação (CENTRA);
– the Slovenian Research Agency through grant P1-0188;
– the Spanish Ministry of Economy (MINECO/FEDER, UE), the Spanish Ministry of Science and Innovation (MICIN), the Spanish Ministry of Education, Culture, and Sports, and the Spanish Government through grants BES-2016-078499, BES-2017-083126, BES-C-2017-0085, ESP2016-80079-C2-1-R, ESP2016-80079-C2-2-R, FPU16/03827, PDC2021-121059-C22, RTI2018-095076-B-C22, and TIN2015-65316-P ('Computación de Altas Prestaciones VII'), the Juan de la Cierva Incorporación Programme (FJCI-2015-2671 and IJC2019-04862-I for F. Anders), the Severo Ochoa Centre of Excellence Programme (SEV2015-0493), and MICIN/AEI/10.13039/501100011033 (and the European Union through European Regional Development Fund 'A way of making Europe') through grant RTI2018-095076-B-C21, the Institute of Cosmos Sciences University of Barcelona (ICCUB, Unidad de Excelencia 'María de Maeztu') through grant CEX2019-000918-M, the University of Barcelona's official doctoral programme for the development of an R+D+i project through an Ajuts de Personal Investigador en Formació (APIF) grant, the Spanish Virtual Observatory through project AyA2017-84089, the Galician Regional Government, Xunta de Galicia, through grants ED431B-2021/36, ED481A-2019/155, and ED481A-2021/296, the Centro de Investigación en Tecnologías de la Información y las Comunicaciones (CITIC), funded by the Xunta de Galicia and the European Union (European Regional Development Fund – Galicia 2014-2020 Programme), through grant ED431G-2019/01, the Red Española de Supercomputación (RES) computer resources at MareNostrum, the Barcelona Supercomputing Centre - Centro Nacional de Supercomputación (BSC-CNS) through activities AECT-2017-2-0002, AECT-2017-3-0006, AECT-2018-1-0017, AECT-2018-2-0013, AECT-2018-3-0011, AECT-2019-1-0010, AECT-2019-2-0014, AECT-2019-3-0003, AECT-2020-1-0004, and DATA-2020-1-0010, the Departament d'Innovació, Universitats i Empresa de la Generalitat de Catalunya through grant 2014-SGR-1051 for project 'Models de Programació i Entorns d'Execució Paralells' (MPEXPAR), and Ramon y Cajal Fellowship RYC2018-025968-I funded by MICIN/AEI/10.13039/501100011033 and the European Science Foundation ('Investing in your future');
– the Swedish National Space Agency (SNSA/Rymdstyrelsen);
– the Swiss State Secretariat for Education, Research, and Innovation through the Swiss Activités Nationales Complémentaires and the Swiss National Science Foundation through an Eccellenza Professorial Fellowship (award PCEFP2_194638 for R. Anderson);
– the United Kingdom Particle Physics and Astronomy Research Council (PPARC), the United Kingdom Science and Technology Facilities Council (STFC), and the United Kingdom Space Agency (UKSA) through the following grants to the University of Bristol, the University of Cambridge, the University of Edinburgh, the University of Leicester, the Mullard Space Sciences Laboratory of University College London, and the United Kingdom Rutherford Appleton Laboratory (RAL): PP/D006511/1, PP/D006546/1, PP/D006570/1, ST/I000852/1, ST/J005045/1, ST/K00056X/1, ST/K000209/1, ST/K000756/1, ST/L006561/1, ST/N000595/1, ST/N000641/1, ST/N000978/1, ST/N001117/1, ST/S000089/1, ST/S000976/1, ST/S000984/1, ST/S001123/1, ST/S001948/1, ST/S001980/1, ST/S002103/1, ST/V000969/1, ST/W002469/1, ST/W002493/1, ST/W002671/1, ST/W002809/1, and EP/V520342/1.

The GBOT programme uses observations collected at (i) the European Organisation for Astronomical Research in the Southern Hemisphere (ESO) with the VLT Survey Telescope (VST), under ESO programmes 092.B-0165, 093.B-0236, 094.B-0181, 095.B-0046, 096.B-0162, 097.B-0304, 098.B-0030, 099.B-0034, 0100.B-0131, 0101.B-0156, 0102.B-0174, and 0103.B-0165; and (ii) the Liverpool Telescope, which is operated on the island of La Palma by Liverpool John Moores University in the Spanish Observatorio del Roque de los Muchachos of the Instituto de Astrofísica de Canarias with financial support from the United Kingdom Science and Technology Facilities Council, and (iii) telescopes of the Las Cumbres Observatory Global Telescope Network.